Numerical modelling of earthquake cycles based on Navier-Stokes equations with Viscoelastic-plasticity rheology

Haibin Yang[1], Louis Moresi[2], Huihui Weng[3], and Julian Giordani[4]

[1]Australian National University
[2]The Australian National University
[3]Nanjing University
[4]Sydney University

February 9, 2023

Abstract

Visco-elastic-plastic modelling approaches for long-term tectonic deformation assume that co-seismic fault displacement can be integrated over 1,000s-10,000s years (tens of earthquake cycles) with the appropriate failure law, and that short-timescale fluctuations in the stress field due to individual earthquakes have no effect on long-term behavior. Models of the earthquake rupture process generally assume that the tectonic (long-range) stress field or kinematic boundary conditions are steady over the course of multiple earthquake cycles. In this study, we develop a numerical framework that embeds earthquake rupture dynamics into a long-term tectonic deformation model by adding inertial terms and using highly adaptive time-stepping that can capture deformation at plate-motion rates as well as individual earthquakes. We reproduce benchmarks at the earthquake timescale to demonstrate the effectiveness of our approach. We then discuss how these high-resolution models degrade if the time-step cannot capture the rupture process accurately and, from this, infer when it is important to consider coupling of the two timescales and the level of accuracy required. To build upon these benchmarks, we undertake a generic study of a thrust fault in the crust with a prescribed geometry. We find that lower crustal rheology affects the periodic time of characteristic earthquake cycles and the inter-seismic, free-surface deformation rate. In particular, the relaxation of the surface of a cratonic region (with a relatively strong lower crust) has a characteristic double-peaked uplift profile that persists for thousands of years after a major slip event. This pattern might be diagnostic of active faults in cratonic regions.

Hosted file

`954409_0_art_file_10626809_rcnvpc.docx` available at https://authorea.com/users/542372/articles/621942-numerical-modelling-of-earthquake-cycles-based-on-navier-stokes-equations-with-viscoelastic-plasticity-rheology

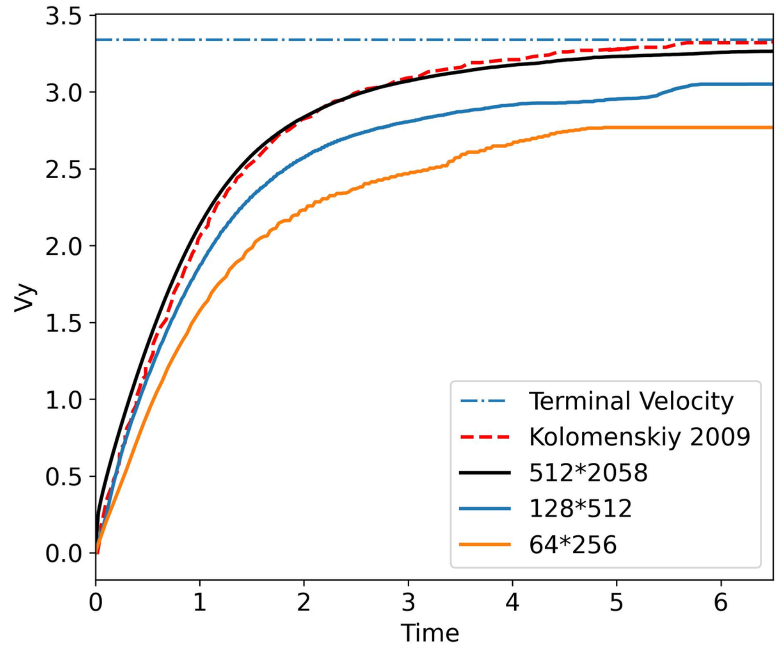
Vy
Time
Terminal Velocity
Kolomenskiy 2009
512*2058
128*512
64*256

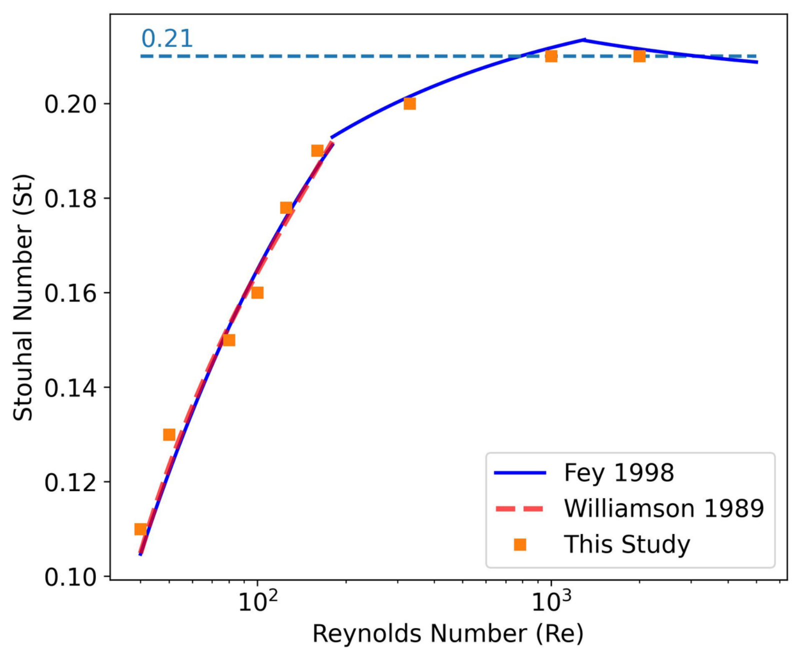
0.21
Stouhal Number (St)
Reynolds Number (Re)
Fey 1998
Williamson 1989
This Study

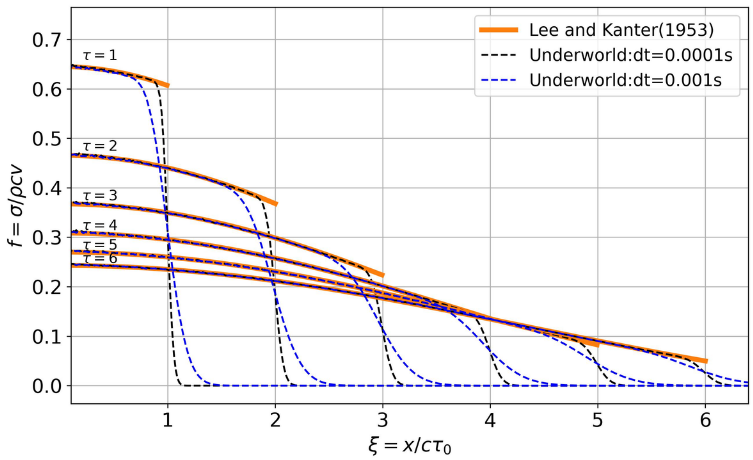
Lee and Kanter(1953)
Underworld:dt=0.0001s
Underworld:dt=0.001s
$f = \sigma/\rho c v$
$\xi = x/c\tau_0$
$\tau = 1$
$\tau = 2$
$\tau = 3$
$\tau = 4$
$\tau = 5$
$\tau = 6$

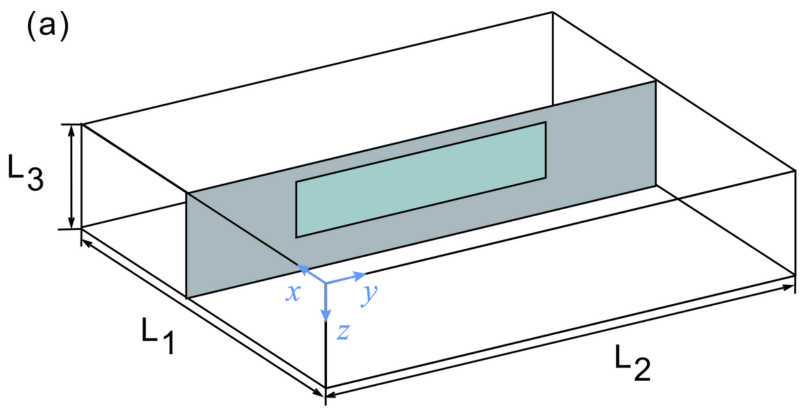
(a)
L3
L1
L2
x
y
z

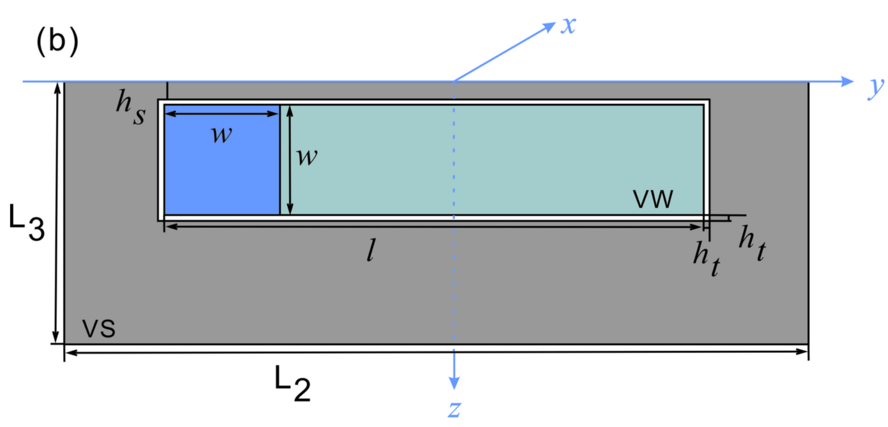
(b)
x
y
z
hs
w
w
VW
l
ht
ht
L3
VS
L2

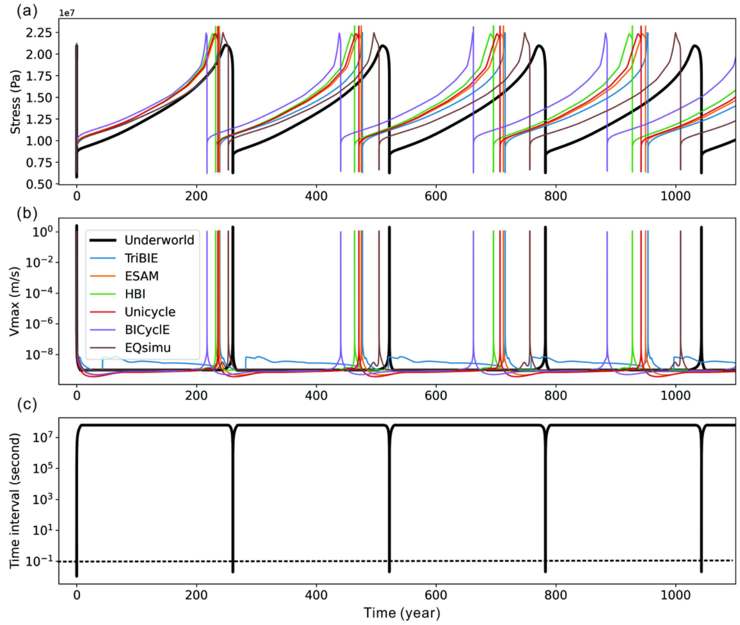

(a)
1e7
Stress (Pa)
(b)
Vmax (m/s)
Underworld
TriBIE
ESAM
HBI
Unicycle
BICyclE
EQsimu
(c)
Time interval (second)
Time (year)

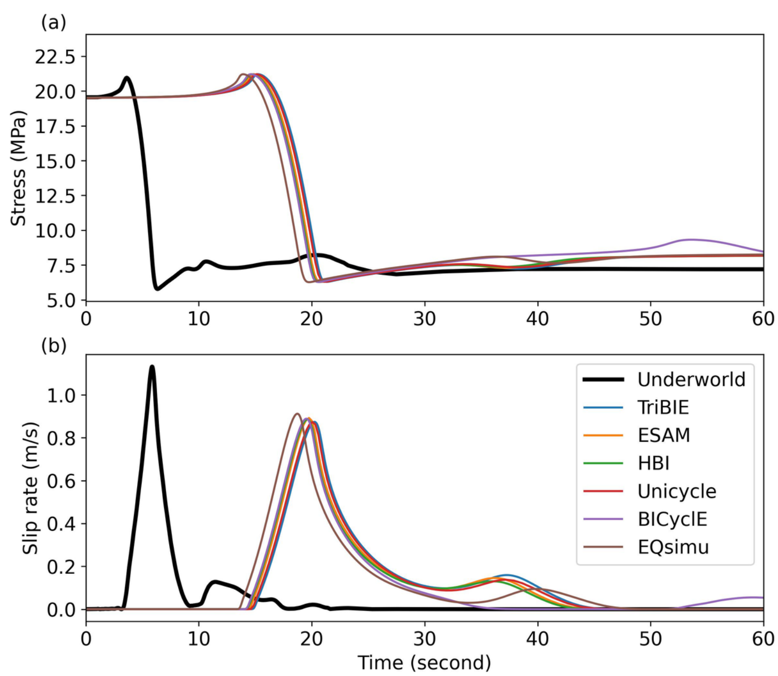

(a)
Stress (MPa)
(b)
Slip rate (m/s)
Underworld
TriBIE
ESAM
HBI
Unicycle
BICyclE
EQsimu
Time (second)

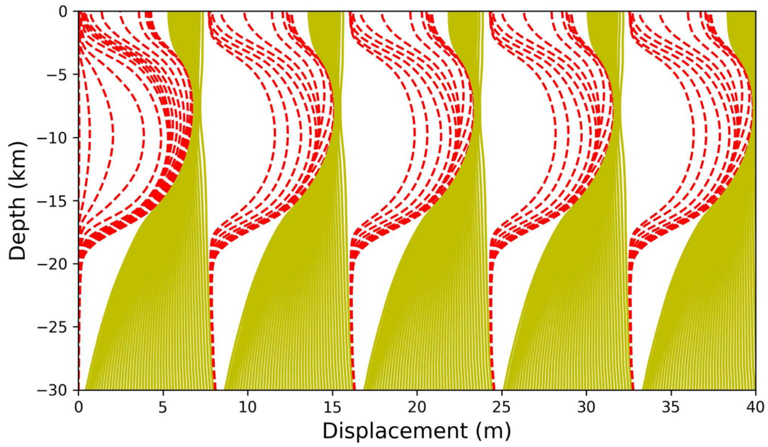
Depth (km)
0
−5
−10
−15
−20
−25
−30
0
5
10
15
20
25
30
35
40
Displacement (m)

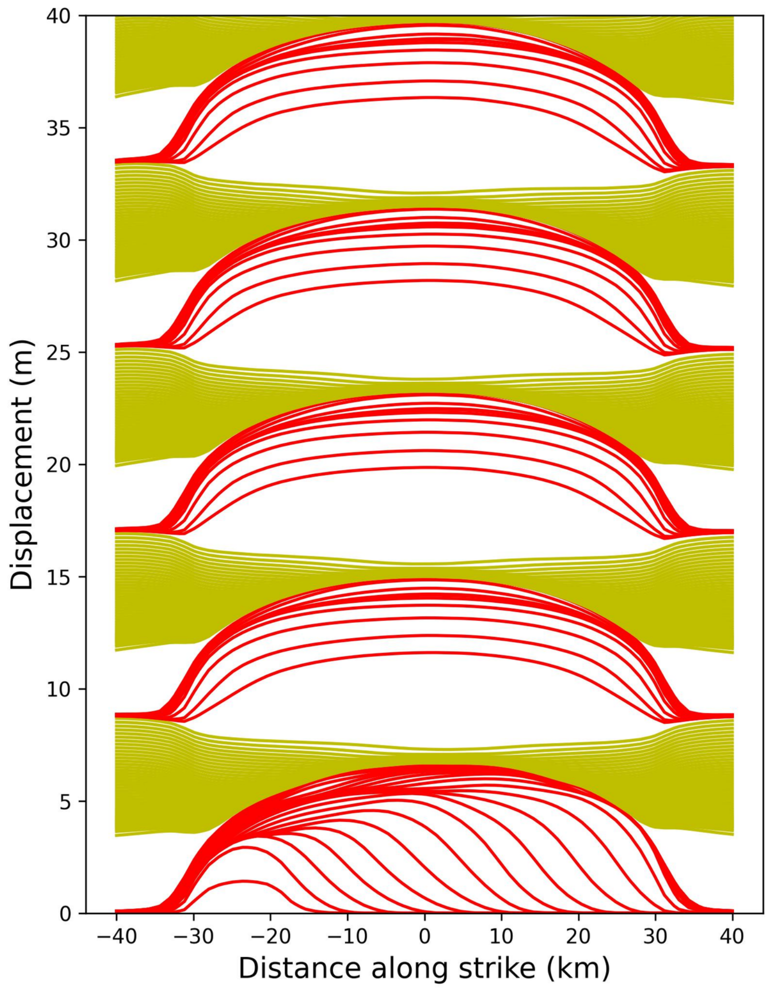
Displacement (m)
Distance along strike (km)
0
5
10
15
20
25
30
35
40
−40
−30
−20
−10
0
10
20
30
40

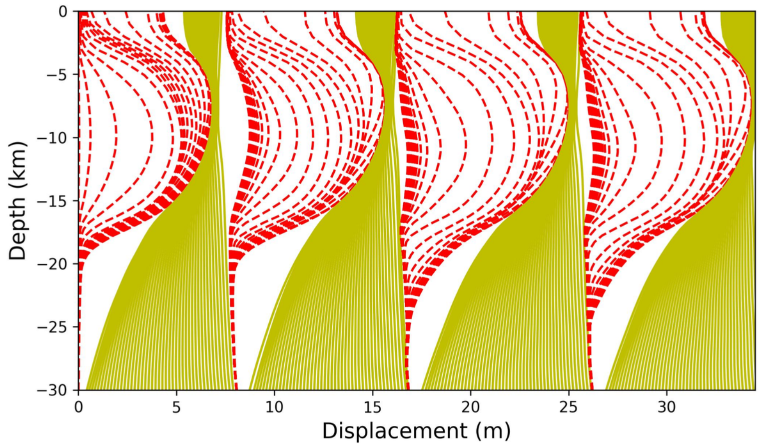
Depth (km)
Displacement (m)
0
−5
−10
−15
−20
−25
−30
0
5
10
15
20
25
30

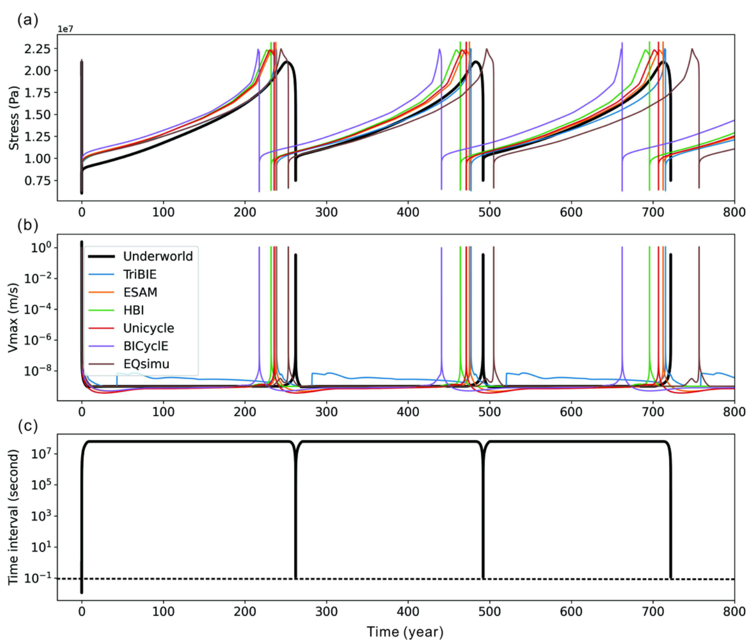
(a)
1e7
Stress (Pa)
(b)
Vmax (m/s)
Underworld
TriBIE
ESAM
HBI
Unicycle
BICyclE
EQsimu
(c)
Time interval (second)
Time (year)

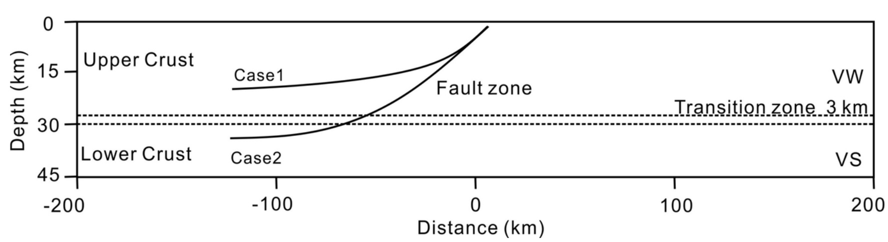
Upper Crust
Case1
Fault zone
VW
Transition zone 3 km
Lower Crust
Case2
VS
Depth (km)
Distance (km)

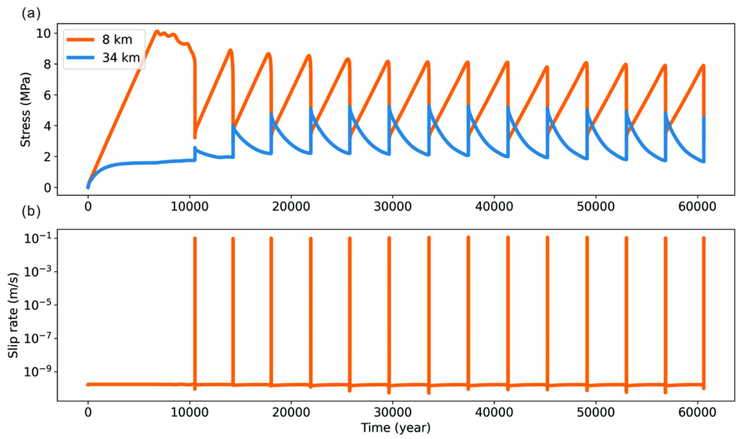

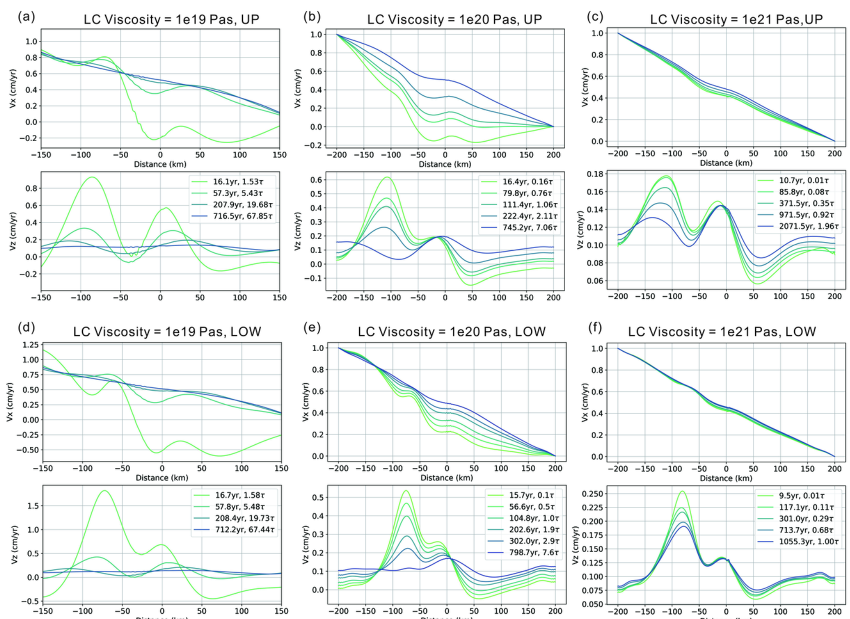

Hosted file

`954409_0_supp_10626762_rmntmb.gif` available at https://authorea.com/users/542372/articles/621942-numerical-modelling-of-earthquake-cycles-based-on-navier-stokes-equations-with-viscoelastic-plasticity-rheology

Hosted file

`954409_0_supp_10626763_rvntvc.gif` available at https://authorea.com/users/542372/articles/621942-numerical-modelling-of-earthquake-cycles-based-on-navier-stokes-equations-with-viscoelastic-plasticity-rheology

Numerical modelling of earthquake cycles based on Navier-Stokes equations with Viscoelastic-plasticity rheology

Haibin Yang[1*], Louis Moresi[1], Huihui Weng[2], Julian Giordani[3]

[1.]Research School of Earth Sciences, Australian National University, Canberra, ACT 0200, Australia

[2.]School of Earth Sciences and Engineering, Nanjing University, Nanjing, China 210023

[3.]School of Geosciences, Sydney University, Sydney, NSW 2006, Australia

*Corresponding author: Haibin.yang@anu.edu.au

Abstract

Visco-elastic-plastic modelling approaches for long-term tectonic deformation assume that co-seismic fault displacement can be integrated over 1,000s-10,000s years (tens of earthquake cycles) with the appropriate failure law, and that short-timescale fluctuations in the stress field due to individual earthquakes have no effect on long-term behavior. Models of the earthquake rupture process generally assume that the tectonic (long-range) stress field or kinematic boundary conditions are steady over the course of multiple earthquake cycles. In this study, we develop a numerical framework that embeds earthquake rupture dynamics into a long-term tectonic deformation model by adding inertial terms and using highly adaptive time-stepping that can capture deformation at plate-motion rates as well as individual earthquakes. We reproduce benchmarks at the earthquake timescale to demonstrate the effectiveness of our approach. We then discuss how these high-resolution models degrade if the time-step cannot capture the rupture process accurately and, from this, infer when it is important to consider coupling of the two timescales and the level of accuracy required. To build upon these benchmarks, we undertake a generic study of a thrust fault in the crust with a prescribed geometry. We find that lower crustal rheology affects the periodic time of characteristic earthquake cycles and the inter-seismic, free-surface deformation rate. In particular, the relaxation of the surface of a cratonic region (with a relatively strong lower crust) has a characteristic double-peaked uplift profile that persists for thousands of years after a major slip event. This pattern might be diagnostic of active faults in cratonic regions.

Plain Language summary:

The numerical modelling method for long-term tectonic deformations averages out the co-seismic fault displacement into thousands to tens of thousands of years, and neglects near-fault damages of earthquakes, therefore may not be able to decipher fault activities in detail. Software simulating earthquake rupture dynamics may not have a good estimation of background stress due to long-term tectonic deformations. This study is aimed to fill the gap between long-term and short-term deformations by modeling earthquake cycles based on Navier-Stokes equations. The inertia term, which is neglected in long-term large-scale modelling methods, is considered to simulate the dynamic rupture processes. The rate-and-state frictional relationship for co-seismic fault slip is implemented in a viscoelastic-plastic earth. Benchmarks of viscous flow, viscoelastic wave propagation and earthquake cycle simulations are tested. Based on these benchmarks, we undertake a generic study of a thrust fault in crust. We find that lower crustal rheology affects the periodic time of characteristic large earthquake cycles and the inter-seismic free surface movement. Cratons with a relatively strong lower crust due to lower temperature remain two peaks in surface uplift profiles around the fault zone for thousands of years after one characteristic earthquake, which help identify active faults in cratons.

Keywords: Earthquake cycles; Navier-Stokes equations; visco-elastic-plastic modelling; adaptive time-stepping; lower crustal strength; active faults in cratons

Key points:

1. We build a code modelling earthquake cycle based on the long-term tectonic modelling software Underworld.

2. Benchmarks at the earthquake timescale are used to demonstrate the effectiveness of our approach.

3. Cratons may remain two peaks in surface uplift profiles near the active fault for >1000 years after one characteristic earthquake.

1 Introduction

Numerical models assume different governing equations and constitutive relations depending on the dominant time- and length-scales for the problem. The timescales associated with changes in whole mantle flow are typically of the order of tens to hundreds of thousands of years and, as a result it is usual to neglect the unimportant inertial terms and it is often unnecessary to consider the effects of elastic stresses. Models are usually formulated on the assumption of creeping viscous flow (the Stokes equations) (McKenzie, 1969). The dynamics of deformation within the lithosphere is dominated by localizing phenomena (shear banding and faulting) that are commonly modelled with a visco-elastic-plastic rheology (Moresi et al., 2007). These models require significantly higher spatial and temporal resolution compared to whole-mantle flow models to capture the stress-redistribution that is associated with the creation, propagation of localized structures and the offsets that occur along their length. Plastic models of localization assume a static equilibrium with any time-dependence resulting from the evolution of damage variables or geometry (e.g., interfaces, surface topography). By contrast, at the shorter timescales associated with the individual ruptures of a fault, the largest terms in the equation of motion come from accelerations and the elastic response of the medium. (Ben‐Zion and Rice, 1993; Rice, 1993; Lapusta et al., 2000).

Fault zones are one of the structural units of the dynamic Earth that is challenging for simulations. Faults accumulate finite strain in deep ductile earth over years or longer and suddenly release stored elastic energy in shallow brittle earth through earthquake ruptures, which cause permanent displacements on the surface. The displacement of faults in long-term tectonic models are averaged over one time step of several millenniums, which approximates the cyclic accumulation of earthquake events. Faults designed in long-term tectonic models have a finite thickness, and are free to deform in geometries, especially for modeling with the Particle-in-cell method (Harlow, 1964; Moresi et al., 2003; Yang et al., 2021a). The long-term tectonic models are driven by speculated external boundary conditions and internal body forces and can evolve in a self-consistent fashion. Conventional models using spectral boundary element method to simulate earthquake kinetics treat earthquake-holding faults as infinite thin interface that are confined to a specific geometry which may not evolve with time (Lapusta et al., 2000; Lapusta and Liu, 2009). The conventional short-term model focuses on one specific earthquake event rather than earthquake cycles. Recent developments with the finite difference, finite element, spectral element, and hybrid methods can flexibly incorporate complex fault geometries at greater computational costs than the boundary element methods which often assume a damped inertia (i.e., 'quasi-dynamic' earthquakes) (Jiang et al. (2022) and references therein). How one fault evolves in response to surface processes and mantle dynamics or interacts with each other in a system is rarely studied (Wang et al., 2012; Sobolev and Muldashev, 2017), especially in a full three-dimensional environment.

To cover the full spectrum of faulting behaviors, one should model both the short- and long-term dynamics. In the past decade, several experiments from the long-term tectonic modelling community have been conducted to develop feasible adaptive models for earthquake-cycle simulation with time steps ranging from sub-seconds to years with viscoelastic materials. Van Dinther et al. (2013) adopted the 2D thermomechanical code I2ELVIS using an implicit, conservative finite difference scheme for incompressible medium (Gerya and Yuen, 2007). This 2D code was further developed for compressible medium by Herrendorfer, Gerya and van Dinter, 2018 (Herrendörfer et al., 2018). On the other hand, Sobolev and Muldshev (2017) develop a similar 2D seismo-thermo-mechanical approach based on SLIM3D (Popov and Sobolev, 2008), which is a thermomechanical finite element code for long-term tectonic modelling, but their experiments limit the minimum modeled time step to minutes such that generation of seismic waves are not studied in their models. Different from previous applications of seismo-thermomechanical models, an elastoplastic code focusing on the shallow brittle part of earth crust was developed by Biemiller and Lavier (2017) to study earthquake cycles of normal faults. Unlike previous modelling of earthquake cycles (Rice, 1993; Lapusta et al., 2000), which assumes fault as an infinite thin interface, experiments developed by Biemiller and Lavier (2017) also allow fault to have a finite thickness as those long-term tectonic models, which have advantages in modelling internal structure evolution of a fault zone.

The frictional constitutive relation is a key factor controlling faulting features. A simplified friction relationship assuming linear decay of friction with steady state velocity was used by Van Dinther et al. (2013), following previous studies (Burridge and Knopoff, 1967; Cochard and Madariaga, 1994; Ampuero and Ben-Zion, 2008). Instead, Biemiller and Lavier (2017), Herrendorer et al. (2018) and Sobolev and Muldshev (2017) use the classical rate-and-state friction (Dieterich, 1978, 1979; Ruina, 1983), which assumes a logarithmic decrease of friction with slip rate. Note that the rate-and-state dependent friction relationship does not include the fracturing mechanism for fault evolution, Tong and Lavier

(2018) develop a new frictional relationship which depends on the historical damage in the fault zone to model quasi-dynamic rupture processes.

In this paper, we discuss our approach to including inertial terms into the open-source Underworld geodynamics modelling framework (Moresi et al., 2007; Mansour et al., 2020), This code was originally designed to address coupled problems in mantle-lithosphere dynamics using a history-dependent, viscoelastic-plastic formulation of the Stokes equations which uses a particle-in-cell approach to tracking elastic stresses during fluid deformation (Moresi et al., 2002; Farrington et al., 2014). Fluid acceleration can also be tracked using the Lagrangian particle swarm which we demonstrate through a series of standard benchmarks of the Navier-Stokes problem. A second benchmark is to compare the speed of a shear-wave through a viscoslastic medium for which analytic solutions are available. In addition, we compare this code with the community code verification exercise for 3D dynamic modelling of sequences of earthquakes and aseismic slip (Jiang et al., 2021). We finally apply our new 3D code for generic models of inter-seismic deformation of thrust faults and discuss how we can use surface geodetic observations to infer the strength of the lower crust and activity of faults in stable cratons.

2 Methods

2.1 Governing equations

We start with the equations for the conservation of momentum (1a) and mass (incompressible material, 1b),

$$\frac{\partial \tau_{ij}}{\partial x_j} - \frac{\partial p}{\partial x_i} = -\rho g_i + \rho \frac{Dv_i}{Dt} \qquad \text{(1a)}$$

$$\frac{\partial v_i}{\partial x_i} = 0 \qquad \text{(1b)}$$

where τ is deviatoric stress, p is pressure, ρ is density, and v is velocity. $\rho \frac{Dv_i}{Dt}$ is the inertia term. In the particle-in-cell method with Lagrangian particles moving between cells, the material derivative of velocity is equal to the time derivative recorded on the material points, and can be approximated by a finite difference expression such as

$$\frac{Dv_i}{Dt} = \frac{\partial v_i}{\partial t} = \frac{v_i - v_i^{t-\Delta t}}{\Delta t} \qquad (2)$$

where Δt is the time interval between the present time, t, and the previous time, $t-\Delta t$; $v_i^{t-\Delta t}$ is the particle velocity from the previous time-step. The mesh-based velocity field is used to update the positions of the particles during a timestep and interpolated to determine the velocity history-variables.

For a viscous material, the constitutive relationship gives

$$\tau_{ij} = 2\eta E_{ij} = \eta(\frac{\partial v_i}{\partial x_j} + \frac{\partial v_j}{\partial x_i}) \qquad (3)$$

where η is the viscosity and E_{ij} is the strain rate. Substituting equation (2) and (3) into (1a), and assuming viscosity is constant, we obtain

$$\eta \frac{\partial^2 v_i}{\partial {x_j}^2} - \rho \frac{v_i}{\Delta t} - \frac{\partial p}{\partial x_i} = -\rho g_i + \rho \frac{-v_i^{t-\Delta t}}{\Delta t} \qquad (4)$$

To solve the unknowns v_i and p, combine equation (1b) and (4) and write them in a matrix form

$$\begin{bmatrix} -\eta \frac{\partial^2}{\partial {x_j}^2} + \frac{\rho}{\Delta t} & \frac{\partial}{\partial x_i} \\ \frac{\partial}{\partial x_i} & 0 \end{bmatrix} \begin{bmatrix} v_i \\ p \end{bmatrix} = \begin{bmatrix} \rho(g_i + \frac{v_i^{t-\Delta t}}{\Delta t}) \\ 0 \end{bmatrix} \qquad (5a)$$

Neglecting the inertia term, the equations (5) can be simplified as a combination of the Stokes equation and continuity equation

$$\begin{bmatrix} -\eta \frac{\partial^2}{\partial {x_j}^2} & \frac{\partial}{\partial x_i} \\ \frac{\partial}{\partial x_i} & 0 \end{bmatrix} \begin{bmatrix} v_i \\ p \end{bmatrix} = \begin{bmatrix} \rho g_i \\ 0 \end{bmatrix} \qquad (5b)$$

2.2 Rheology

2.2.1 Maxwell viscoelastic constitutive equations

The Maxwell material assumes that the strain rate tensor, E, is a sum of an elastic strain rate tensor E^e, a viscous strain rate tensor E^v:

$$E_{ij} = E_{ij}^e + E_{ij}^v = \frac{\tau_{ij}'}{2G} + \frac{\tau_{ij}}{2\eta} \qquad (7)$$

where G is shear modulus, and η is viscosity. Writing the stress derivative τ_{ij}' in form of an approximate difference:

$$\tau'_{ij} \approx \frac{\tau_{ij}-\tau_{ij}^{t-\Delta t}}{t-\Delta t} \qquad (8)$$

gives

$$\tau_{ij} = 2\,\frac{\eta G\Delta t}{\eta+ G\Delta t}\left[E_{ij} + \frac{\tau_{ij}^{t-\Delta t}}{2G\Delta t}\right] \qquad (9)$$

where τ is current stress solution at time, t, and the stress $\tau^{t-\Delta t}$ at earlier time, $t-\Delta t$. The equation (9) can be written in a form of equation (3)

$$\tau_{ij} = 2\eta^{ev}E^{ev} \qquad (10)$$

where

$$\eta^{ve} = \frac{\eta G\Delta t}{\eta+G\Delta t} \qquad (11a)$$

$$E^{ve} = E_{ij} + \frac{\tau_{ij}^{t-\Delta t}}{2G\Delta t} \qquad (11b)$$

Substituting equation (10) into equation (1a) leads to

$$2\eta^{ve}\frac{\partial^2 v_i}{\partial {x_j}^2} - \frac{\partial p}{\partial x_i} = -\rho g_i + \rho\frac{Dv_i}{Dt} - \frac{\eta^{ve}}{G\Delta t}\frac{\partial}{\partial x_j}\tau_{ij}^{t-\Delta t} \qquad (12)$$

Combined with equation (1b), the equation (12) can be reformulated as

$$\begin{bmatrix} -\eta\dfrac{\partial^2}{\partial {x_j}^2} + \dfrac{\rho}{\Delta t} & \dfrac{\partial}{\partial x_i} \\ \dfrac{\partial}{\partial x_i} & 0 \end{bmatrix}\begin{bmatrix} v_i \\ p \end{bmatrix} = \begin{bmatrix} \rho g_i + \rho\dfrac{v_i^{t-\Delta t}}{\Delta t} + \dfrac{\eta^{ve}}{G\Delta t}\dfrac{\partial}{\partial x_j}\tau_{ij}^{t-\Delta t} \\ 0 \end{bmatrix} \qquad (5c)$$

Equations (5a, 5b and 5c) have the same matrix form as

$$\begin{bmatrix} \boldsymbol{K} & \boldsymbol{G} \\ \boldsymbol{G^T} & \boldsymbol{0} \end{bmatrix}\begin{bmatrix} \boldsymbol{v} \\ \boldsymbol{p} \end{bmatrix} = \begin{bmatrix} \boldsymbol{F} \\ \boldsymbol{0} \end{bmatrix} \qquad (5d)$$

where $\boldsymbol{K}$ is conventionally taken as the stiffness matrix, $\boldsymbol{G}$ is the discrete gradient operator and $\boldsymbol{F}$ is known as the force term.

2.2.2 Yield strength for long-term deformation

The Drucker-Prager yield model is used to simulate long-term fault behavior:

$$|\tau| < \tau_{yield} = \mu_{st}^{*}p + C \qquad (13)$$

where the upper limit of the second invariant of the stress tensor is τ_{yield} , C is rock cohesion and μ^*_{st} is static friction coefficient commonly used in long-term deformation. With the plastic deformation, the plastic strain rate tensor E^p needs to be added to equation (7):

$$E_{ij} = E^e_{ij} + E^v_{ij} + E^p_{ij} \qquad (14)$$

The composite visco-elastic-plastic flow material is modelled with an effective viscosity:

$$\eta_{vep} = \min\left(\eta^{ve}, \frac{\tau_{yield}}{2E^{ve}_{II}}\right) \qquad (15)$$

where the E^{ve}_{II} is the second invariant of the effective strain rate in equation (11b).

2.2.3 Rate-and-state frictional relationship

For the short-term deformation, e.g., the earthquake rupture time scale, the rate-and-state frictional (RSF) relationship is commonly used in the earthquake rupture simulations (Dieterich, 1978, 1979; Ruina, 1983). The dynamic friction coefficient

$$\mu^* = \mu^*_{st} + a \cdot ln\left(\frac{v}{v_0}\right) + b \cdot ln\left(\frac{\theta v_0}{D_{RS}}\right) \qquad (16)$$

where a and b are nondimensional parameters, v is the slip velocity on the fault, D_{RS} is the characteristic slip distance, θ is the state variable, μ^*_{st} and v_0 are the reference friction coefficient and reference velocity (usually assumed to be the far-field plate boundary velocity), respectively. $a - b < 0$ represents strength weakening material, in which earthquake nucleation is favored; $a - b > 0$ represents a strength strengthening material which tends to prevent earthquake ruptures from propagating. The evolution of state θ is a function of slip rate v and critical slip distance L

$$\frac{d\theta}{dt} = 1 - \frac{\theta v}{D_{RS}} \qquad (17)$$

If the slip rate v is constant over a time step, a finite difference approximateion of equation (17) can be written

$$\theta = \frac{D_{RS}}{v} + \left(\theta^{t-\Delta t} - \frac{D_{RS}}{v}\right) e^{-\frac{\Delta t v}{D_{RS}}} \qquad (18)$$

where θ is the value of the state variable at the current time, t, and $\theta^{t-\Delta t^e}$ is the value at the earlier time, $t - \Delta t$. In numerical implementations, the fault slip rate is approximated by $2E_{II}w_f$, where E_{II} is the second invariant of the strain rate of the fault zone and the w_f is the fault zone width. θ is updated after each time step with updated fault slip rate.

Same as the form of equation (13), the yielding stress can be written as

$$|\tau| < \tau_{yield} = \mu^* p + C \qquad (19)$$

Note that co-seismic slip rate is several orders of magnitude higher than the inter-seismic fault creep rate. The rate-and-state frictional relationship is conventionally used for co-seismic fault movement. In our numerical modelling, both the co-seismic and inter-seismic friction coefficient are modelled with the rate-and-state frictional relationship (Eq. 16). That means, for the inter-seismic stage, the fault movement is in a quasi-equilibrium state with $\frac{dv}{dt} \approx 0$ and $\frac{d\theta}{dt} \approx 0$. If the slip rate $v \approx v_0$ and $v_0 = \frac{D_{RS}}{\theta}$, $\mu^* = \mu_{st}^*$ and the yielding stress in Eq. 19 converges to Eq. 13.

2.3 Adaptive time step

For long-term and short-term deformations, we calculate various time step limits and choose the minimum at each iteration. First, the time step should be smaller than the characteristic Maxwell relaxation time:

$$\Delta t_{ve} = \eta / G \qquad (20)$$

Assuming $G = 3 \times 10^{10}\ Pa$ and $\eta = 10^{20}\ Pas$ gives a relaxation time of ~ 100 years. For the viscoelastic-plastic deformation, the viscoplastic viscosity defined as

$$\eta_{vp} = \eta \frac{\tau_{II}}{2\eta E_{II}^p + \tau_{II}} \qquad (21)$$

where τ_{II} and $E_{II}^p$is the second invariant of the deviatoric stress and plastic strain rate, respectively. Note that if $E_{II}^p = 0$, $\eta_{vp} = \eta$. Replacing η in equation (20) with η_{vp} in equation (23), we have

$$\Delta t_{vep} = \eta_{vp} / G \qquad (24)$$

In addition, the Courant-Friedrichs-Lewy (CFL) condition is also used for the stability of the dynamic rupture simulations. Under this condition, the slip per time step is not allowed to be larger than the grid size Δx or Δy:

$$\Delta t_{CFL} = \min\left(\left|\frac{\Delta x}{v_x}\right|, \left|\frac{\Delta y}{v_y}\right|\right) \quad (25)$$

Then, we set a maximum time step allowed in one time step, Δt_{max} = 10 years.

Therefore, the minimum time step for the model is

$$\Delta t_0 = £ \min[\Delta t_{vep}, \Delta t_{CFL}, \Delta t_{max}] \quad (26)$$

where the pre-factor £ is a constant value and is set to be 0.2 in most cases in this study. Because too small Δt would make our solver unstable, we thus truncate the minimum time step by

$$\Delta t = \max[\Delta t_0, \Delta t_{min}] \quad (27)$$

and Δt_{min}= 0.01s in this study. To reflect the weakening of the weakening of the state variable, Lapusta et al. (2000) and Herrendorfer et al. (2018) also limit the time step by $\Delta t_w = \varphi \frac{D_{RS}}{v}$, where the pre-factor φ is a constant. Herrendorfer et al. (2018) find Δt_w is very close to Δt_{vep} during co-seismic stages. We thus only consider Δt_{vep} in our study and use the pre-factor £ to tune the value of the viscoelastic-plastic relaxation time. See more discussion on the time stepping procedures in following sections.

3 Benchmarks

In this section, several benchmarks are investigated to demonstrate the effectiveness of our code in modelling coupled simulations: (1) time-dependent viscous flow compared with published numerical solutions, (2) analytical solutions for viscoelastic wave propagation and (3) community model of earthquake cycle simulations.

3.1 Time-dependent viscous flow

The inertia term is important in earthquake dynamic rupture processes, which can reach the same order of magnitude as gravity acceleration but is neglected in long-term tectonic modeling. We first test the implemented inertia term (Eq. 1) with published numerical results from Kolomenskiy and Schneider (2009), which is a fluid-solid interaction model where an infinite-long solid cylinder body falls perpendicularly to its longitudinal axis. The modelled fluid viscosity η = 0.03926, fluid density ρ= 1, solid cylinder density ρ_s= 2, gravity acceleration g=9.81 and the diameter of the cylinder D = 1. The model size is Lx×Ly = 10×40, and the different model resolutions 512×2058, 256×1024, 128×252 and 64×256 quadrilateral bilinear elements are tested for comparison. The cylinder starts from rest and then speeds up its falling speed due to gravity before reaching a steady state (Fig. 1).

Considering the balance between drag and buoyance-corrected weight, the terminal steady state velocity u_t can be estimated by

$$C_d \frac{\rho ut^2}{2} D + (\rho - \rho_s) g \frac{\pi D^2}{4} = 0 \qquad (28)$$

where C_d is the drag coefficient, which is a function of Reynolds number, *Re* $(= \frac{\rho u_t D}{\eta})$, for a cylinder falling in a steady inflow.

The choice of parameters gives a terminal velocity u_t = 3.34 with the corresponding *Re* = 85. Our numerical models with high mesh resolution also agrees with this estimated terminal velocity (Fig. 1) to within 5% for the same mesh resolution (512× 2058). The high-resolution models are also comparable to results from Kolomenskiy and Schneider (2009). Reducing mesh resolution also reduces the modelled falling velocity. The terminal velocity is dropped by ~20% when the mesh resolution is reduced by a factor of 8 in each direction. For the viscous inertia flow that can generate eddies, the *Re* is estimated to be >~10. We test a group of benchmarks with Re=40-2000 to see how well our numerical results are matched by published solutions in a quantitative fashion. Here we introduce another dimensionless parameter Strouhal number, *St* = fD/U, where f is the frequency of vortex shedding, D is the characteristic length (e.g., the diameter of the falling cylinder in above mentioned experiment), and U the fluid velocity. No analytical solutions are available for the comparison, but many studies have provided different approximations of *St* for *Re* of different ranges (Fey et al., 1998; Williamson and Brown, 1998). Our numerical results are visually comparable with previous studies (Fig. 2). We note that precision of modelling results depends on the mesh resolution as shown in Fig. 1. That is because high *Re* produces very small-scale eddies to dissipate the energy, thus requiring higher mesh resolution to capture more detailed structures. Examples of two cases with *Re*=40 and 400 are shown in supplementary material as videos. As flow passes a fixed cylinder, the vortical wake develops for high *Re* values, and it is unstable and forms the von Karman vortex street due to oscillating forces (see Supplementary material).

3.2 Viscoelastic wave radiation

During the dynamic earthquake rupture propagation, the stored elastic energy is partly released by elastic wave propagation. The radiated seismic waves have also been demonstrated to trigger earthquake events on distant faults when the triggering stress is higher than the required fault failure stress (Brodsky and van der Elst, 2014). We evaluate how well the dynamic stress changes, after a wave passes through, can be described by our numerical model.

For a quantitative comparison with the analytical solution, here we first consider a simple case, an infinite long rod made up of a linear Maxwell material and the x coordinate is measured along the rod length. A 2D numerical model with high aspect ratio is used to simulate the infinite long rod. The model size Lx × Ly = 1100 m × 4.68 m and is simulated with 800×3 quadrilateral quadratic elements. The periodic boundary condition is applied in y direction. Initially, the rod is unstrained and at rest, and then it is subjected to a constant shear velocity V at one end x = 0. The analytical solution for stress $\sigma(x,t)$ is provided by Lee and Kanter (1953),

$$\sigma = -\rho c V e^{-\left(\frac{\gamma G}{2}\right)t} I_o \left[\frac{\gamma G}{2}\left(t^2 - \frac{x^2}{c^2}\right)^{\frac{1}{2}}\right] H\left(t - \frac{x}{c}\right) \qquad (29)$$

Where I_o is the Bessel function of imaginary argument and H is the Heaviside step function, γ is the reciprocal of the viscosity, G is the shear modulus, and $c^2 = G/\rho$. We scale the time by characteristic relaxation time, $\tau = t/\tau_0 = t\gamma G$, and the distance by $\xi = \gamma G x/c = x/c\tau_0$, and equation (29) becomes

$$-\frac{\sigma}{\rho c V} = f \; = e^{-\frac{\tau}{2}} I_0 \left[\frac{1}{2}(\tau^2 - \xi^2) H(\tau - \xi)\right] \qquad (30)$$

In Fig. 3, the dimensionless stress f is plotted against dimensionless distance ξ for the dimensionless time τ between 0 and 8 and it illustrates the propagation and decay of the stress wave from the shear end of the rod in the case of a Maxwell material in dimensionless units. The Heaviside step function H shows the wave front is at $\tau = \xi$, and the stress is zero ahead of this front. If the unit velocity of the wave front in the (ξ, τ) system is transformed back into the physical (x, t) system, the front of the disturbance moves with the elastic wave velocity c. Note that a wave of stress discontinuity of amplitude -ρcV sets out from shear boundary x=0, and the stress discontinuity is of magnitude -ρcV$e^{-\xi/2}$ when it reaches ξ. That is, the stress magnitude dies out exponentially as wave progresses and the stress at the shear boundary x=0 also falls off as the duration of shearing increases.

Comparing our results with the analytical solution, we find our numerical solution well describes the stress field behind the wave front and disperses at the stress discontinuity. The dispersion effect of the wave front makes it difficult to pick the arrival time of seismic waves, thus making it hard to determine the seismic wave velocity. This dispersion effect can be damped by reducing the time step at the cost of computational time as the smaller time step produces steeper stress profile at wave front (Fig. 3). To roughly estimate the seismic wave velocity, the wave front is better represented by the time that corresponds the maximum of the stress derivative with time (ξ = 1,2,3...n, and n is an integer number; Fig. 3).

3.3 3D model simulation of earthquake cycles with the RSF

To further benchmark this code, we compare it with the community benchmark model BP5 (Jiang et al., 2022) for three-dimensional dynamic modelling of sequences of earthquakes and aseismic slip (3D SEAS) simulations. Adding the inertia term in the momentum balance equation (Eq. 1) and using the Maxwell material (Eq. 7), our code can simulate earthquake cycles for brittle materials by implementing artificially high viscosity (>10^{25} Pas) of long relaxation time (>1 million years). Full descriptions of this benchmark are available online on the SEAS code comparison platform (https://strike.scec.org/cvws/seas/), and here we give a brief introduction.

A vertical, strike-slip fault is embedded in the central part of a homogeneous and isotropic half-space, with a free surface z = 0 (Fig. 4). The finite width of the fault is of one element size in x direction. The fault-normal, along-strike and along-dip dimensions of the computational model is marked as L1, L2, and L3, respectively. A constant rate V_L is applied at the bottom of the model across the finite fault zone and a constant fault-parallel velocity ($\pm$½ V_L) is also applied at the far field of the fault at x = $\pm$½ L1. To achieve a spatially uniform distribution of fault slip rates, the initial state over the entire fault zone is prescribed with the steady-state value at the initiate slip rate V_{init}, that is $\theta_0 = \frac{D_{RS}}{V_{init}}$. The corresponding steady-state pre-stress τ^0 is

$$\tau^0 = a\sigma_n arcsinh\left[\frac{V_{init}}{2V_0}\exp\left(\frac{\mu_0 + b\ln\left(\frac{V_0}{V_{init}}\right)}{a}\right)\right] \quad (31)$$

A nucleation location for the first event is designed to break the lateral symmetry of the fault and facilitate code comparisons. The nucleation zone is located within the velocity weakening region with a width of w = 12 km and a center at (-24 km, -10 km). In this nucleation zone, a higher initial slip rate V_i is applied in y direction at t = 0, and the initial state variable θ_0 is kept unchanged, thus producing a higher pre-stress by replacing V_{init} with V_i in Eq. 31.

There are two critical length scales in earthquake dynamics: the cohesive zone and the nucleation zone. The former describes the spatial region near the rupture front where breakdown of fault resistance occurs and shrinks as rupture propagates (Palmer and Rice, 1973) and the latter describes the minimum region for spontaneous nucleation on a fault controlled by velocity-weakening friction (Rice and Ruina, 1983; Rubin and Ampuero, 2005). For rate-and-state friction law, the static cohesive zone Λ_0 is estimated as follows (Day et al., 2005; Lapusta and Liu, 2009):

$$\Lambda_0 = C\frac{GD_{RS}}{b\sigma_n} \tag{32}$$

where C is a pre-factor of order 1. And the size of nucleation zone is estimated for the aging law for 0.5<a/b<1 as follows (Chen and Lapusta, 2009):

$$h = \frac{\pi}{2}\frac{GbD_{RS}}{(b-a)^2\sigma_n} \tag{33}$$

The calculated cohesive zone and nucleation zone for the BP5 benchmark model are 5.6 km and 12.5 km, respectively. To have sufficient resolution, we use ~1000 m as the grid size in low-order accuracy for BP5, which resolves the cohesive zone with no less than four cells, as suggested by Day et al. (2005).

The BP5 benchmark is first simulated with a reference model size of 96 km (L1)$\times$ 100 km (L2)$\times$30 km (L3) by 128$\times$64$\times$64 quadrilateral bilinear elements. Results from the SEAS code comparison platform (https://strike.scec.org/cvws/seas/) with the mesh resolution of 1000 m are selected for comparison in this study (Table 2). The stress at depth of 10 km in the middle point along the fault strike (y = 0) and the maximum slip rate along the entire fault is tracked for comparison (Fig. 5). 0.1m/s is taken as a threshold of fault slip rate to mark the earthquake initiation. In case of long-term fault behavior, the period of earthquake cycles in Underworld is ~260 years, which is longer than other published results of ~230 years but is very close to the estimation from EQsimu. Both Underworld and EQsimu use the Finite element method while other codes are based on the (spectral) boundary element method. The stress drop after each event is ~10 MPa and is consistent with all other results. Regarding the short-term behavior, the stress and slip rate at the reference point (0, 0, -10 km) are investigated (Fig. 6). The rupture propagation speed in Underworld is much faster than other results. The estimated time of earthquake rupture propagation from the nucleation zone to the reference point is ~5s in the Underworld models, and ~20s in the other models. The fast rupture propagation in Underworld may be attributed to two reasons. First, all other models consider quasi-static situations while Underworld is fully dynamic modelling. The V_{max} in Fig. 5b and slip rate in Fig. 6b show higher slip rate in Underworld than other models and the seismic wave radiation may produce higher rupture propagation rate than the quasi-static codes which damp the inertia term.

Both the long-term and short-term fault slip evolution is recorded by vertical (Fig. 7) and horizontal (Fig. 8) profiles. The maximum co-seismic slip for each event is ~7 m and consistent with published results (Jiang et al., 2021). The designed weak zone at y=-30-18 km can nuclearize the initial earthquake rupture (Fig. 8) for the first event but fails in the sequential events. Comparing with the published data (Fig.8 in Jiang et al., 2021), we find a gap zone of fault slip (white area in the VW zone; z = -4 to -16 km in Fig. 7 and y=-30 to 30km in Fig. 8) between the defined seismic and aseismic slip. Such a gap is not observed in the published data. The gap zone in Underworld means the supposed seismic slip (defined by a threshold slip rate of 0.01 m/s) has experienced slow slip at the VW zone (<0.01 m/s) before earthquake rupture initiates. We consider such slow slip events to be numerical artifacts since we begin to fill this gap when we adopt a shorter time step than the reference model (Fig. 9). On the other hand, a model with a slightly longer time step than the reference model is also tested (Fig. 10). The minimum time step used here is longer than 0.1s (see the dashed line in Fig. 10c) while that in the reference model is shorter than 0.1s (see the dashed line in Fig. 5c). With a longer timestep, the period of earthquake cycles is ~230 years, almost the same as other modelling results. The shorter period of earthquakes than the reference model may be caused by lower stress drop after earthquakes, which results from the use of longer time steps. The extreme case is that, if a time step longer than the Maxwell relaxation time is used, there would be no earthquake events and thus no stress drops in the viscoelastic media. Therefore, the choice of time step is very crucial to fault behavior, especially for the short-term dynamics. The stress change during an earthquake also affects the long-term earthquake cycles in numerical calculations.

In this benchmark, the vertical fault is conformed to one element, and the fault material is not mixed with wall rocks in any elements. We further test models with a fault of one and a half element width, and do not find intensive stress fluctuations as is common for particle-in-cell methods when elements are filled with materials of high viscosity contrast (Yang et al., 2021a). We find the stress field is also comparable with that of community models, but the maximum slip rate is almost twice of that from community models. This might be due to the calculation of fault slip rate by $2E_{II}w_f$. Although the fault is designed to be of 1.5 element width, only central parts of the fault zone occupy one element, and both fault-wall rock interfaces are in elements containing two materials. Better ways to estimate the effective strain rate for the entire fault zone (Yang et al., 2021a) may address this issue but is beyond the topic of this study.

4 Case study of thrust fault earthquakes

4.1 Model description

Thrust fault earthquakes happening on a non-planar fault plane is common in nature. It can be a bent subduction zone in inter-plate boundaries or an intraplate décollement fault. A two-dimensional (2D) crustal model (Fig. 11), 400-km long and 45-km wide, with a curved fault is designed to investigate generic behaviors of earthquake cycles with 720×96 quadrilateral bilinear elements. The finite fault zone thickness is of about 6 element size. Two cases of different cutting depth of the décollement fault are investigated. The fault geometry can be described by a parabolic equation, $z=(D_{top}-D_{base})/x_0^2(x-x_0)^2+D_{top}$, where D_{base} (at $x=x_0$) and D_{top} (at $x=0$) is the deepest and shallowest depth of the fault, respectively. One case has a D_{base} at a depth of 24 km while the other model has a D_{base} at a depth of 33 km, with x_0=-120 km for both cases. They are, respectively, referred to as UP and LOW models based on the cutting depth. The VW zone extends from surface to a depth of 27 km, VS zone is from 30 km to the base at a depth 45 km and a transition zone of 3-km thick is in between (Fig. 11). The entire fault in UP model is located within the VW zone in upper crust while LOW model cuts into the VS zone in lower crust. The fault zone has a distinctly low theta value (0.029 years) from wall rocks (1.9e16 years) to localize the deformation. Detailed parameters of this 2D model are listed in Table 3. A relatively high viscosity (10^{27} Pas) is applied to upper crust material, and the upper crust is supposed to be dominated by elastic deformation. The viscosity of lower crust ranging from 10^{19} Pas to 10^{21} Pas is used to see how the strength of lower crust affects earthquake cycles. This study focuses on the inter-seismic deformation of the free surface, which can be detected by geodetic observations. To make it easier to identify these models, we name different models after the cutting depth and lower crustal viscosity. For example, the UP model with a lower crust viscosity of 10^{21} Pas is named UP21.

4.2 Results

These models share some common evolution features, and we use the UP21 model as an example to demonstrate some generic patterns of earthquake cycles (Fig. 12). The model is initially free of stress and the shear stress in upper crust linearly increases with a constant strain rate. The stress in upper crust is limited by the yielding stress of the rock, which is estimated to be 9 MPa with a constant normal stress of 30 MPa and static frictional coefficient of 0.3. The stress in the lower crust is limited by the viscosity and strain rate. The first event happens after 10,000 years, which is longer than the characteristic relaxation time of lower crustal material (~1000 years). The lower crustal stress almost linearly increases in the first 1000 years, and then slows down with time. It approaches the upper limit of ~1.8 MPa, which approximates 2V/Lη, where V = 1cm/year, L = 400 km and η = 10^{21} Pas. After several (3-4) cycles, the stress evolves in a periodic way with a time interval between two sequential events of ~3800 years. The slip rate of the shallower reference point at a depth of 8 km crosses more than 8 orders of magnitude, with the co-seismic slip rate of ~0.1 m/s and inter-seismic slip rate $<10^{-9}$ m/s. Regarding the period of earthquake cycles for UP models, we find the period decreases with lower crustal viscosity. The period for UP20 is ~3100 years and ~2100 years for UP19.

Fig. 13 illustrates the influence of the lower crustal viscosity on inter-seismic movement of the free surface. It is summarized as follows:

1. In terms of the Vx in both UP and LOW models, for the time no longer than a hundred years after one characteristic earthquake event, there are clearly perturbations above the fault zone (x = -100 km - 50 km) for models with lower crustal viscosity of 10^{19}Pas and 10^{20} Pas but not for higher crustal viscosity. After hundreds of years, there are almost no differences in Vx for models with different lower crustal strength and a linear trend occurs across the fault plane.

2. In terms of the Vz in both UP and LOW models, all the models demonstrate clear signals related to fault movement, but the absolute magnitude at the same time after one earthquake event decays with the lower crustal viscosity.

3. In LOW models, there is one major peak and one sub-peak. The major peak is located at x=~-80 km, the depth of which is the joint of the VW-VS transition zone

and the fault plane. The sub-peak is located around x= 0 km, which is the fault trace on the surface. In LOW20 (Fig. 13e), the sub-peak develops with time, while major peak decays with time. In the long run (time>7 τ), the major peak at x =-80 km may disappear, and the sub-peak at x=0 starts to dominate the deformation.

4. In UP models, the two-peak pattern observed in LOW models are observable as well. In contrast to LOW models, the major peak (left one) appears not at x=-80 km but shifts leftward to ~120 km (except for the LOW19 model), corresponding to the leftmost tip of the fault zone. The sub-peak is located around x=0 km as well. The major peak at x = -120 km decays with time as that in LOW models, but the sub-peak at x=0 km almost does not change with time.

5. Peak patterns in model UP21(Fig. 13c) differ from other models in terms of the magnitude differences. For the time no longer than a hundred years after one characteristic earthquake event, the magnitude of sub-peaks is more than two thirds of the major peak. The sub-peaks in other models are generally less than half of the major peak.

4.3 Geodynamic and seismic hazard indications

Different cases illustrated in Fig. 11 may represent faults in different tectonic settings. The LOW models may represent mature faults cutting through the entire brittle upper crust into lower crust. The UP models may represent immature or shallow faults that are located within brittle upper crust. Any downward propagation of earthquake ruptures in LOW models may be stopped by VS zone due to high temperature in lower crust (Scholz, 1998) and the rupture propagation in UP models can be interrupted by high strength material or zones of low stress state near the down tip of the fault zone (Yang et al., 2021b). In structure geology, fault zones in LOW models can be the dominant faults of a thick-skinned structure where the basement is involved in deformation (Rodgers, 1949), while that UP models can be a thin-skinned structure where only surficial sediments are deformed (Rodgers, 1949).

Our models show that inter-seismic surface movement in both LOW and UP models are affected by lower crustal rheology. Generally, vertical uplift rate provides a more sensitive signal to lower crustal viscosity than horizontal slip rate. The major peak of the uplift rate profile after less than a hundred years corresponds to the lowermost point of the rupture in VW zone, which provides one way to estimate the potential rupture width for a characteristic earthquake. As the periodic time of earthquake cycles is also affected by lower crust viscosity, study areas with good constraints on frictional strength and normal stress on the fault plane, the periodic time of earthquake cycles can be used to infer the lower crustal viscosity. This provides an independent estimation of the lower crustal viscosity from conventional methods (Shi et al., 2015; Yang et al., 2020; Wang et al., 2021).

The model UP21 has a brittle upper crust of 30 km, viscosity in lower crust of 1e21 Pas and the average strain rate in the crust is ~10^{-16} 1/s. These settings are typical for stable cratons. Shallow earthquakes are also common in stable cratons. For example, earthquakes in cratonic continents in Australia and India are detected to be located less than 10 km deep below surface (Yang et al., 2021b; Jackson and McKenzie, 2022). These so-called stable continents also produce destructive earthquakes (Yang et al., 2021b); For example, the 1556 Huaxian earthquake (M 8.0), the deadliest earthquake in human history that killed 830,000 people, occurred in the middle of continental China. Seismic quiescent may in some cases relate to short instrumental histories (< ~150 years) with respect to the earthquake cycles (>1000 years). For the characteristic earthquakes in stable continents, the model UP21 suggests that the Vx is not sensitive to fault activity at all, but the vertical displacements remain two peaks for more than 2000 years. The peak value in UP21 is > 1 mm/yr, that is still detectable for the state-of-the-art geodetic survey methods (Hao et al., 2014).

5 Conclusions

We build a code modelling earthquake cycle based on the Underworld software, which is designed for long-term large-scale tectonic simulations. The inertia term is first added, and the Navier-Stokes function is benchmarked against publications of viscous inertia flow modelling. Numerical solution calculated by Underworld for wave propagation in materials of Maxwell rheology is also compared with analytical solutions. These results suggest high mesh resolution and small timestep enables excellent agreements between Underworld solutions and other published numerical results or analytical solutions.

We further implement the rate-and-state frictional relationship for co-seismic fault slip in a visco-elastic-plastic model. A 3D earthquake cycle model is built to compare with results from the community code verification exercise for 3D dynamic modelling of sequences of earthquakes and aseismic slip. Although the Underworld code assumes incompressible material, it reproduces comparable periodic time of earthquake cycles, stress drop change after an earthquake event and co-seismic slip to the community code verification exercise. A relatively fast rupture propagation speed in Underworld may be attributed to Underworld considering fully dynamic rupture while others quasi-dynamic models. The variable time stepping procedures are important in affecting transitions from aseismic (or slow slip) to seismic slip. It deserves further exploration in future work.

A curved thrust fault cutting to lower crust or located in brittle upper crust is investigated to see how lower crustal viscosity affects inter-seismic surface motion. Without changing the prescribed velocity boundary condition, increasing lower crustal viscosity tends to increase the periodic time of earthquake cycles and decrease the magnitude of vertical motion rate. Two peaks are common in inter-seismic surface uplift profile across a reverse fault. The major peak, far from the fault trace, indicates the end point of the fault in the velocity weakening zone, and decays with time; the sub-peak is near the fault trace and almost remains unchanged. Shallow active faults in cratons with a strong lower crust is supposed to be detected by geodetic observations of uplift patterns around fault traces, where two peaks are of comparable magnitude.

References

Ampuero, J.P., Ben-Zion, Y., 2008. Cracks, pulses and macroscopic asymmetry of dynamic rupture on a bimaterial interface with velocity-weakening friction. Geophysical Journal International 173, 674-692.

Barbot, S., 2021. A spectral boundary ‐ integral method for quasi ‐ dynamic ruptures of multiple parallel faults. Bulletin of the Seismological Society of America 111, 1614-1630.

Ben ‐ Zion, Y., Rice, J.R., 1993. Earthquake failure sequences along a cellular fault zone in a three ‐ dimensional elastic solid containing asperity and nonasperity regions. Journal of Geophysical Research: Solid Earth 98, 14109-14131.

Biemiller, J., Lavier, L.L., 2017. Earthquake supercycles as part of a spectrum of normal fault slip styles. Journal of Geophysical Research: Solid Earth 122, 3221-3240.

Brodsky, E.E., van der Elst, N.J., 2014. The uses of dynamic earthquake triggering. Annual Review of Earth Planetary Sciences 42, 317-339.

Burridge, R., Knopoff, L., 1967. Model and theoretical seismicity. Bulletin of the seismological society of america 57, 341-371.

Chen, T., Lapusta, N.J.J.o.G.R.S.E., 2009. Scaling of small repeating earthquakes explained by interaction of seismic and aseismic slip in a rate and state fault model. 114.

Cochard, A., Madariaga, R., 1994. Dynamic faulting under rate-dependent friction. pure applied geophysics 142, 419-445.

Day, S.M., Dalguer, L.A., Lapusta, N., Liu, Y., 2005. Comparison of finite difference and boundary integral solutions to three‐dimensional spontaneous rupture. Journal of Geophysical Research: Solid Earth 110.

Dieterich, J.H., 1978. Time-dependent friction and the mechanics of stick-slip, Rock friction and earthquake prediction. Springer, pp. 790-806.

Dieterich, J.H., 1979. Modeling of rock friction: 1. Experimental results and constitutive equations. Journal of Geophysical Research: Solid Earth 84, 2161-2168.

Farrington, R.J., Moresi, L.N., Capitanio, F.A., 2014. The role of viscoelasticity in subducting plates. Geochem Geophy Geosy 15, 4291-4304.

Fey, U., König, M., Eckelmann, H., 1998. A new Strouhal–Reynolds-number relationship for the circular cylinder in the range 47< Re< 2× 10 5. Physics of Fluids 10, 1547-1549.

Gerya, T.V., Yuen, D.A., 2007. Robust characteristics method for modelling multiphase visco-elasto-plastic thermo-mechanical problems. Physics of the Earth and Planetary Interiors 163, 83-105.

Hao, M., Wang, Q., Shen, Z.K., Cui, D., Ji, L., Li, Y., Qin, S., 2014. Present day crustal vertical movement inferred from precise leveling data in eastern margin of Tibetan Plateau. Tectonophysics 632, 281-292.

Harlow, F.H., 1964. The particle-in-cell computing method for fluid dynamics. Methods Comput. Phys. 3, 319-343.

Herrendörfer, R., Gerya, T., Van Dinther, Y., 2018. An Invariant Rate‐ and State‐Dependent Friction Formulation for Viscoeastoplastic Earthquake Cycle Simulations. Journal of Geophysical Research: Solid Earth 123, 5018-5051.

Jackson, J., McKenzie, D., 2022. The exfoliation of cratonic Australia in earthquakes. Earth Planetary Science Letters 578, 117305.

Jiang, J., Erickson, B.A., Lambert, V.R., Ampuero, J.P., Ando, R., Barbot, S.D., Cattania, C., Zilio, L.D., Duan, B., Dunham, E.M., 2022. Community‐driven code comparisons for three‐dimensional dynamic modeling of sequences of earthquakes and aseismic slip. Journal of Geophysical Research: Solid Earth 127, e2021JB023519.

Kolomenskiy, D., Schneider, K., 2009. A Fourier spectral method for the Navier–Stokes equations with volume penalization for moving solid obstacles. Journal of Computational Physics 228, 5687-5709.

Lapusta, N., Liu, Y., 2009. Three‐dimensional boundary integral modeling of spontaneous earthquake sequences and aseismic slip. Journal of Geophysical Research: Solid Earth 114.

Lapusta, N., Rice, J.R., Ben‐Zion, Y., Zheng, G., 2000. Elastodynamic analysis for slow tectonic loading with spontaneous rupture episodes on faults with rate‐and state‐dependent friction. Journal of Geophysical Research: Solid Earth 105, 23765-23789.

Lee, E.H., Kanter, I., 1953. Wave propagation in finite rods of viscoelastic material. Journal of applied physics 24, 1115-1122.

Li, D., Liu, Y.J., 2016. Spatiotemporal evolution of slow slip events in a nonplanar fault model for northern Cascadia subduction zone. Journal of Geophysical Research: Solid Earth 121, 6828-6845.

Liu, D., Duan, B., Luo, B., 2020. EQsimu: a 3-D finite element dynamic earthquake simulator for multicycle dynamics of geometrically complex faults governed by rate-and state-dependent friction. Geophysical Journal International 220, 598-609.

Mansour, J., Giordani, J., Moresi, L., Beucher, R., Kaluza, O., Velic, M., Farrington, R.J., Quenette, S., Beall, A.P., 2020. Underworld2: Python geodynamics modelling for desktop, hpc and cloud. Journal of Open Source Software 5, 1797.

McKenzie, D.P., 1969. Speculations on the Consequences and Causes of Plate Motions*. Geophysical Journal International 18, 1-32.

Moresi, L., Dufour, F., Muhlhaus, H.B., 2002. Mantle convection modeling with viscoelastic/brittle lithosphere: Numerical methodology and plate tectonic modeling. Pure and Applied Geophysics 159, 2335-2356.

Moresi, L., Dufour, F., Muhlhaus, H.B., 2003. A Lagrangian integration point finite element method for large deformation modeling of viscoelastic geomaterials. Journal of Computational Physics 184, 476-497.

Moresi, L., Quenette, S., Lemiale, V., Meriaux, C., Appelbe, B., Muhlhaus, H.B., 2007. Computational approaches to studying non-linear dynamics of the crust and mantle. Physics of the Earth and Planetary Interiors 163, 69-82.

Ozawa, S., Ida, A., Hoshino, T., Ando, R., 2021. Large-scale earthquake sequence simulations of 3D geometrically complex faults using the boundary element method accelerated by lattice H-matrices on distributed memory computer systems. arXiv preprint arXiv:.12165.

Palmer, A.C., Rice, J.R., 1973. The growth of slip surfaces in the progressive failure of over-consolidated clay. Proceedings of the Royal Society of London. A. Mathematical Physical Sciences 332, 527-548.

Popov, A.A., Sobolev, S.V., 2008. SLIM3D: A tool for three-dimensional thermomechanical modeling of lithospheric deformation with elasto-visco-plastic rheology. Physics of the earth planetary interiors 171, 55-75.

Rice, J.R., 1993. Spatio‐temporal complexity of slip on a fault. Journal of Geophysical Research: Solid Earth 98, 9885-9907.

Rice, J.R., Ruina, A.L., 1983. Stability of steady frictional slipping.

Rodgers, J., 1949. Evolution of thought on structure of middle and southern Appalachians. AAPG Bulletin 33, 1643-1654.

Rubin, A.M., Ampuero, J.P., 2005. Earthquake nucleation on (aging) rate and state faults. Journal of Geophysical Research: Solid Earth 110.

Ruina, A., 1983. Slip instability and state variable friction laws. Journal of Geophysical Research: Solid Earth 88, 10359-10370.

Scholz, C.H., 1998. Earthquakes and friction laws. Nature 391, 37-42.

Segall, P., Bradley, A.M., 2012. The role of thermal pressurization and dilatancy in controlling the rate of fault slip. Journal of Applied Mechanics 79.

Shi, X.H., Kirby, E., Furlong, K.P., Meng, K., Robinson, R., Wang, E., 2015. Crustal strength in central Tibet determined from Holocene shoreline deflection around Siling Co. Earth and Planetary Science Letters 423, 145-154.

Sobolev, S.V., Muldashev, I.A., 2017. Modeling seismic cycles of great megathrust earthquakes across the scales with focus at postseismic phase. Geochemistry, Geophysics, Geosystems 18, 4387-4408.

Tong, X., Lavier, L.L., 2018. Simulation of slip transients and earthquakes in finite thickness shear zones with a plastic formulation. Nature communications 9, 1-8.

Van Dinther, Y., Gerya, T.V., Dalguer, L.A., Mai, P.M., Morra, G., Giardini, D., 2013. The seismic cycle at subduction thrusts: Insights from seismo‐thermo‐mechanical models. Journal of Geophysical Research: Solid Earth 118, 6183-6202.

Wang, K., Hu, Y., He, J.H., 2012. Deformation cycles of subduction earthquakes in a viscoelastic Earth. Nature 484, 327-332.

Wang, M., Shen, Z.K., Wang, Y., Bürgmann, R., Wang, F., Zhang, P.Z., Liao, H., Zhang, R., Wang, Q., Jiang, Z.S., 2021. Postseismic deformation of the 2008 Wenchuan earthquake illuminates lithospheric rheological structure and dynamics of eastern Tibet. Journal of Geophysical Research: Solid Earth 126, e2021JB022399.

Williamson, C.H.K., Brown, G.L., 1998. A series in $1/\sqrt{Re}$ to represent the Strouhal–Reynolds number relationship of the cylinder wake. Journal of Fluids Structures 12, 1073-1085.

Yang, H., Moresi, L.N., Mansour, J., 2021a. Stress recovery for the particle-in-cell finite element method. Physics of the Earth Planetary Interiors 311, 106637.

Yang, H., Moresi, L.N., Quigley, M., 2020. Fault spacing in continental strike-slip shear zones. Earth Planetary Science Letters 530, 115906.

Yang, H., Quigley, M., King, T.R., 2021b. Surface slip distributions and geometric complexity of intraplate reverse-faulting earthquakes. GSA Bulletin.

Figures

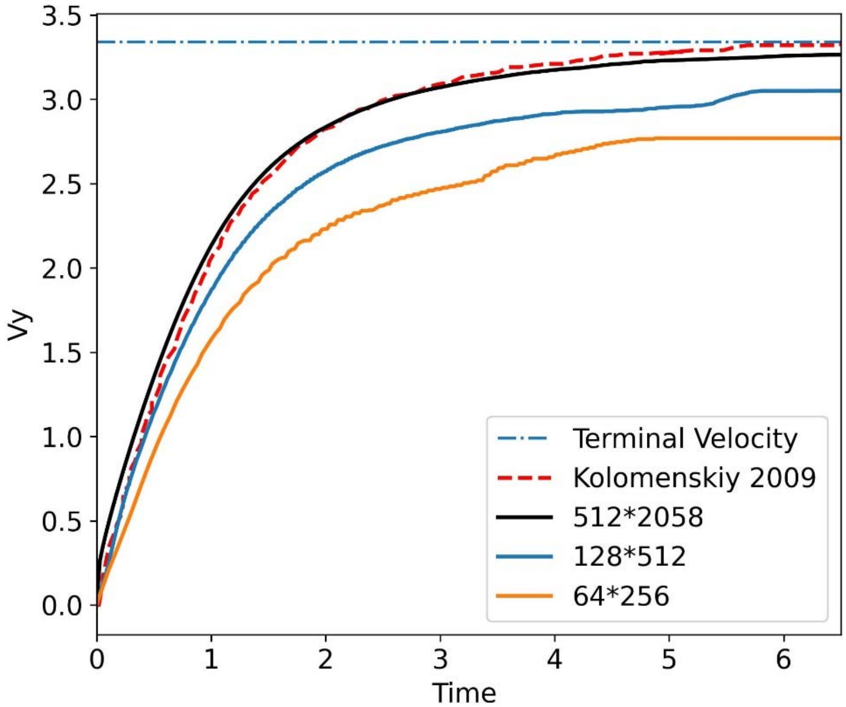

Figure 1. Velocity of a falling cylinder starting from rest to steady state.

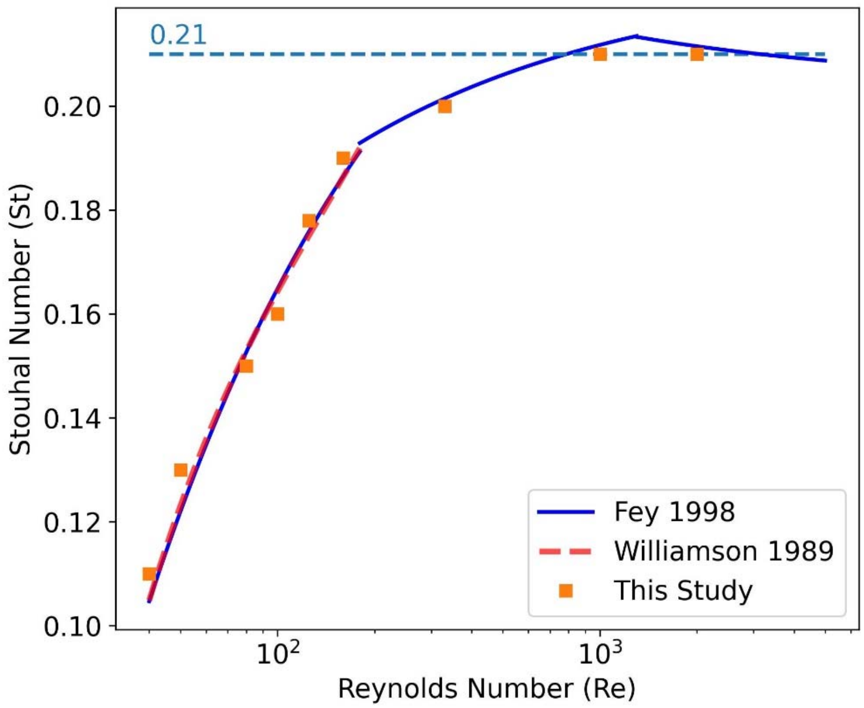

Figure 2. Strouhal number versus Reynolds number. Note that the estimation from Williamson and Brown (1998) almost overlaps with Fey et al. (1998) in the range of 40-150. For 10000>Re>200, the Strouhal number is estimated to be around 0.21.

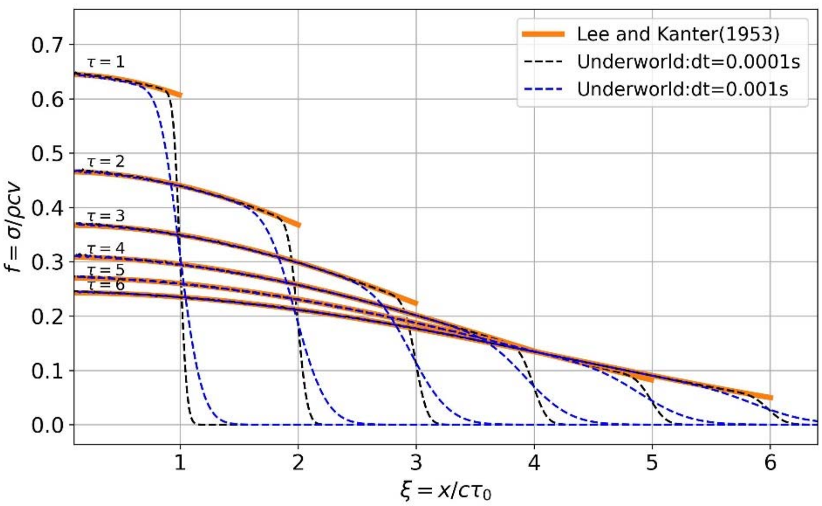

Figure 3. Wave propagation along a Maxwell rod.

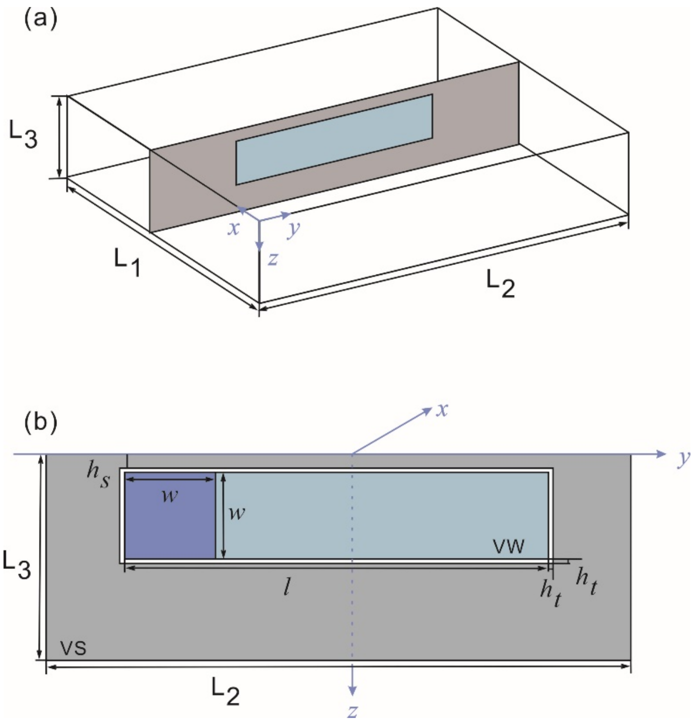

Figure 4. The benchmark model BP5 for 3D sequence of earthquakes and aseismic slip modelling. (a) A vertical planar fault is embedded in the middle of a homogenous, isotropic half-space with a free surface at z=0. Fault behavior is controlled by the rate-and-state friction law. A periodic boundary condition is applied in y direction. (b) The velocity-weakening (VW) region (dark and light blue) is located within a transition zone (white), outside of which is the velocity-strengthening (VS) region (grey). In y and z directions, the frictional domain and velocity-weakening region are (L2, L3) and (l, w), respectively. An initial nucleation zone (dark blue square with a width of w) is designed at the left end of the velocity-weakening region.

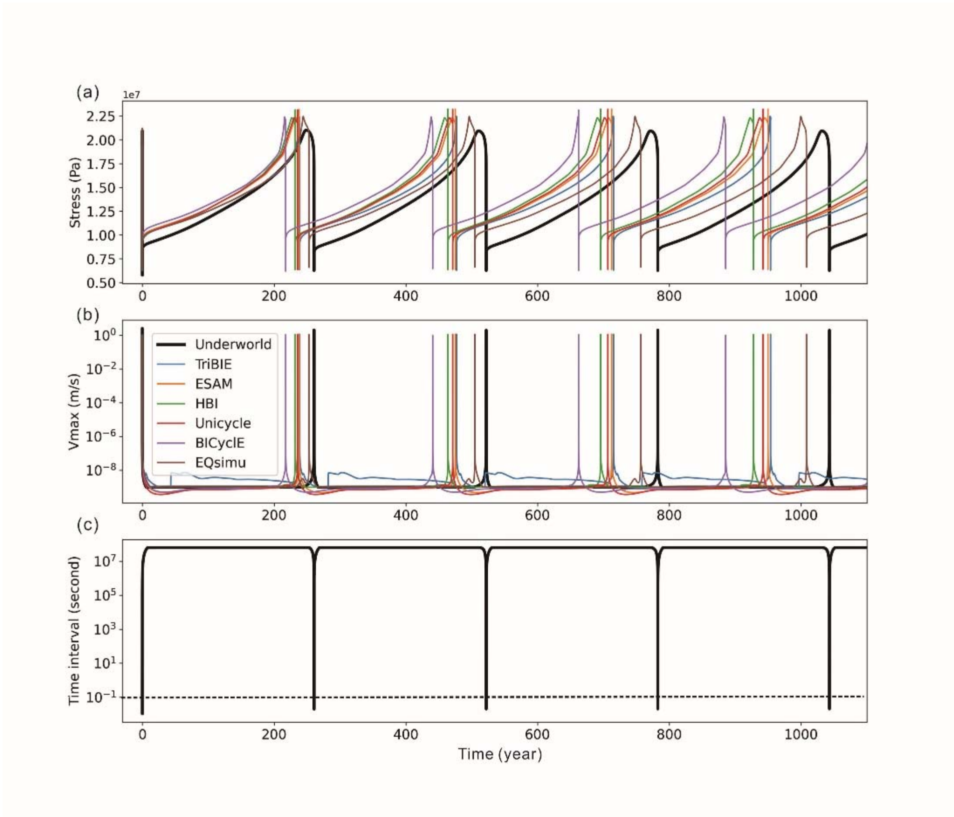

Figure 5. Evolution of the stress at the reference point (0, 0, -10 km) (a), maximum slip rate along the entire fault zone (b) and the adaptive time step used in simulation (c) for the reference model.

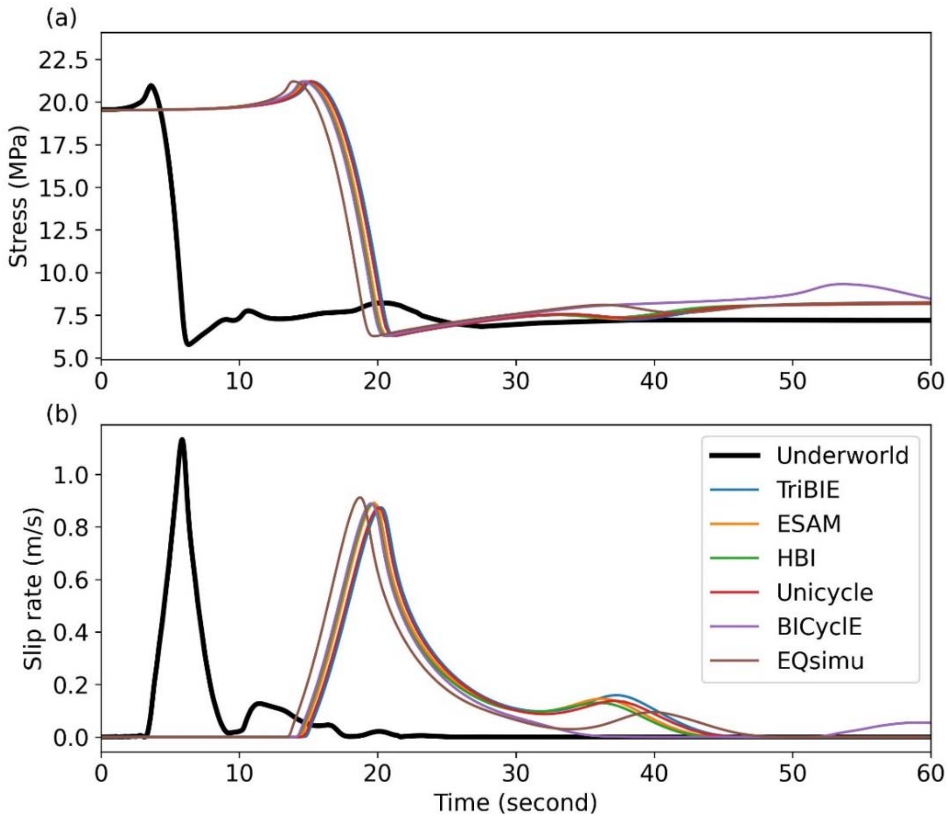

Figure 6. Stress (a) and slip rate (b) at the reference point (0, 0, -10 km) for the first 60 seconds since the initiation of the first event.

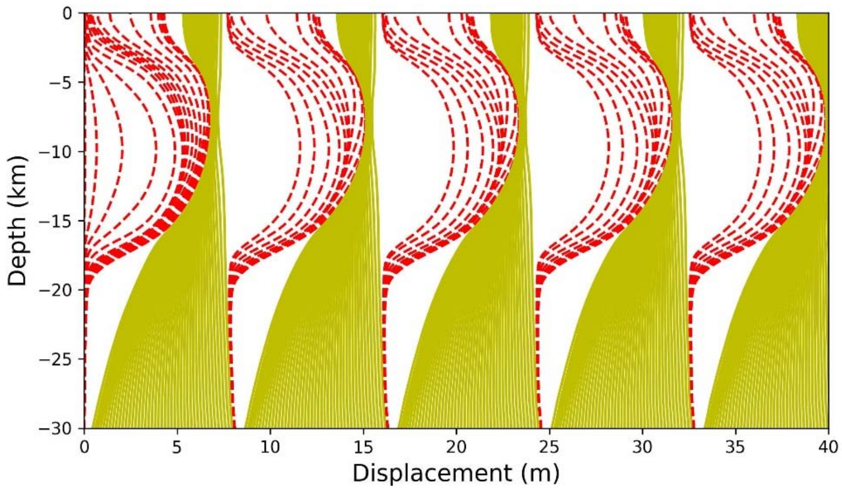

Figure 7. Cumulative fault slip evolution along a vertical profile (y = 0 km). The seismic slip (red lines) is plotted every 1 second and aseismic slip (yellow lines) is plotted every 5 years, with the threshold slip rate V_{th} = 0.01 m/s.

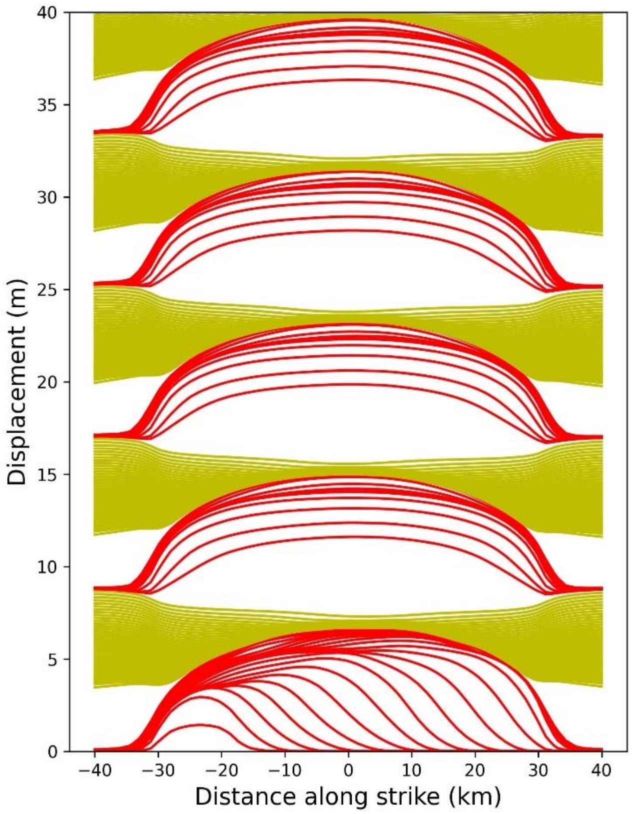

Figure 8. Cumulative fault slip evolution along a horizontal profile (z = -10 km). The seismic slip (red lines) is plotted every 1 second and aseismic slip (yellow lines) is plotted every 5 years, with the threshold slip rate V_{th} = 0.01 m/s.

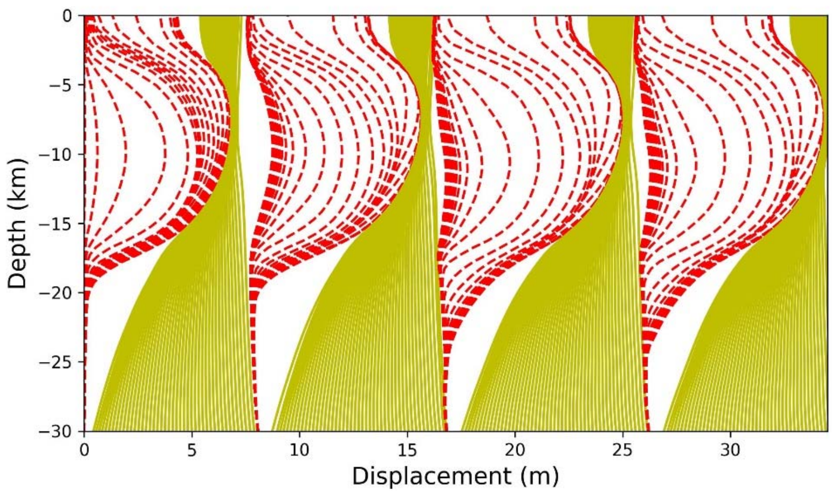

Figure 9. Cumulative fault slip evolution along a vertical profile (y = 0 km) with a shorter time step than the reference model. The seismic slip (red lines) is plotted every 1 second and aseismic slip (yellow lines) is plotted every 5 years, with the threshold slip rate V_{th} = 0.01 m/s.

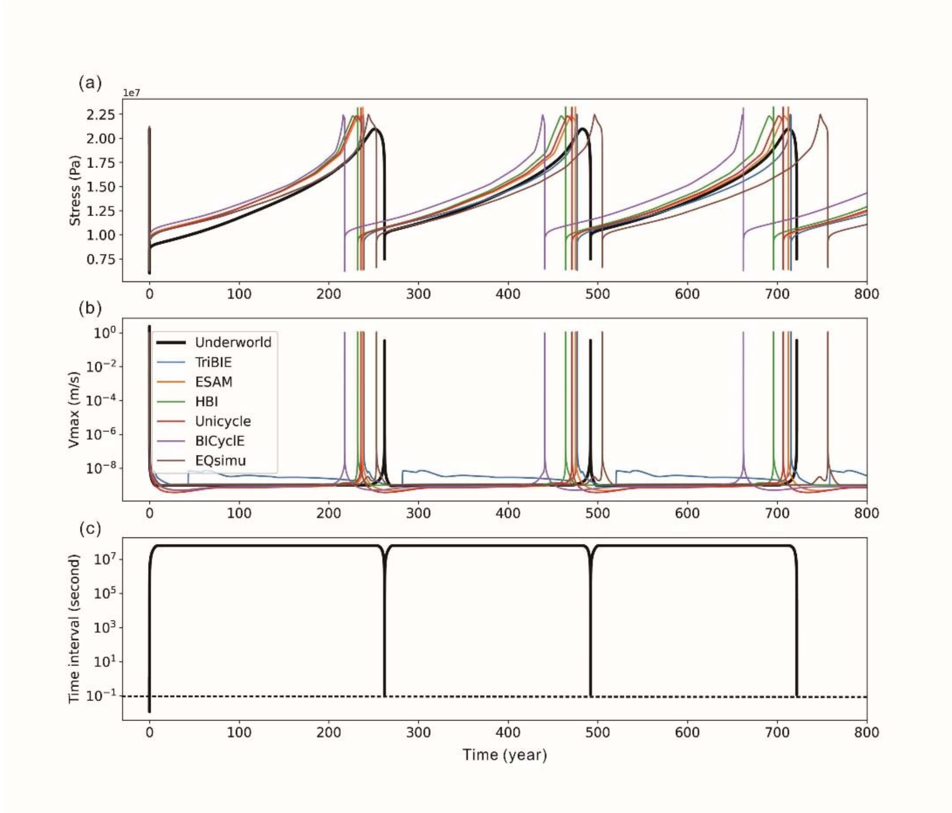

Figure 10. Evolution of the stress at the reference point (0, 0, -10 km) (a), maximum slip rate along the entire fault zone (b) and the adaptive time step used in simulation (c) for the model with longer time step than the reference model.

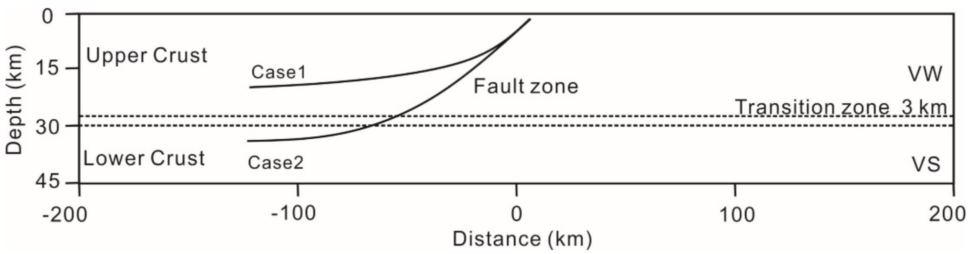

Figure 11. Setup of a two-dimensional crustal model with a free surface on top and free slip boundary condition on base. The right boundary is fixed, and the left boundary is applied with a constant velocity of 1 cm/year. Two cases of a fault zone, UP (case1) and LOW (case2), have distinct cutting depth in crust.

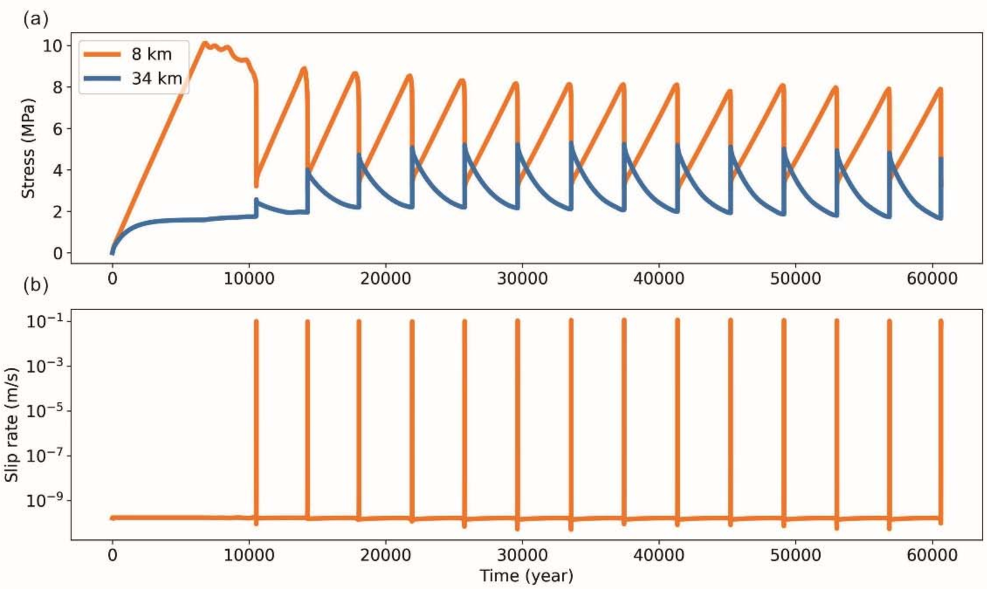

Figure 12. Evolution of the stress at the reference point at a depth of 8 km (orange) and 33 km (blue) in the fault zone (a) and slip rate (only for the shallow point) (b) for UP model with the lower crust viscosity of 1e21 Pas, referred as model UP21.

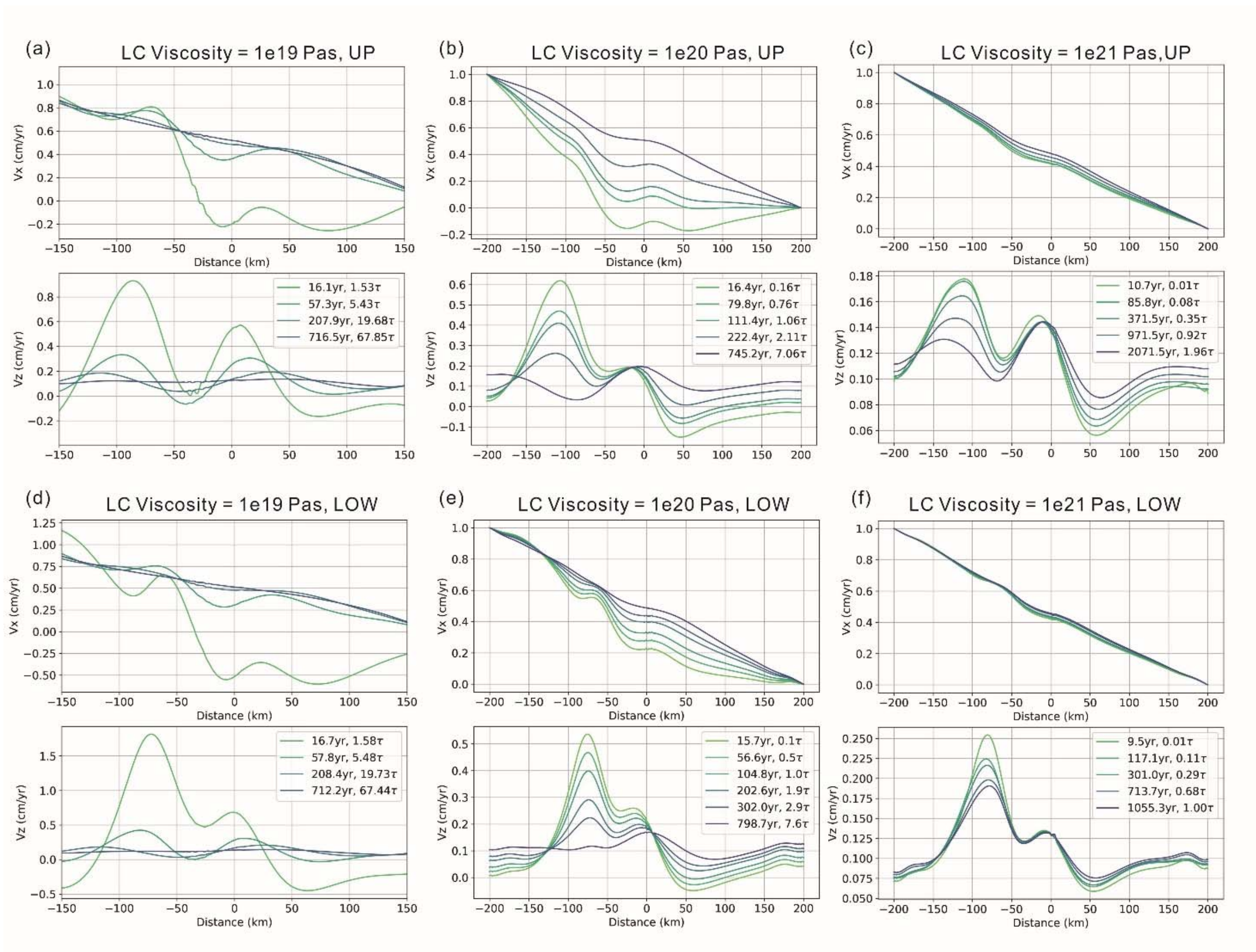

Figure 13. Horizontal (Vx) and vertical (Vz) inter-seismic movement at the top surface of the UP (a-c) and LOW (d-f) models. The lower crustal viscosity of 10^{19} Pas (a & d), 10^{20} Pas (b & e) and 10^{21} Pas (c &f) for each case illustrates how lower crustal viscosity affects inter-seismic deformations. The legend represents the absolute time (left column) and the time relative to the characteristic relaxation time τ (right column).

Tables

Table 1 Parameters in Benchmark Model BP5

Parameter	Symbol	Value in BP5
Density	ρ	2670 kg/m3
Shear wave speed	Cs	3.464 km/s
Effective normal stress	σ_n	25 MPa
Characteristic state evolution distance	D_{RS}	0.14 m/0.13 m (nucleation zone)
Rate-and-state parameter, VW	a	0.004
Rate-and-state parameter, VS	a	0.04
Rate-and-state parameter, VW & VS	b	0.03
Reference slip rate	V_0	10^{-6} m/s
Reference coefficient of friction	μ_{st}^*	0.6
Plate loading rate	V_L	10^{-9} m/s
Initial slip rate	V_{init}	10^{-9} m/s
Initial slip rate in nucleation zone	V_i	0.03 m/s
VW-VS transition zone width	h_t	2 km
VW zone width	w	12 km
VW zone length	l	60 km
Shallow VS region width	h_s	2 km
Nucleation zone width	w	12 km

Table 2 Codes used in comparison of BP5 benchmark model

Code Name	Type	Simulation name	Reference
BICyclE	SBEM	Lambert	Lapusta and Liu (2009)
TriBIE	BEM	Li D.	Li and Liu (2016)
Unicycle	BEM	Barbot	Barbot (2021)
HBI	BEM	Ozawa	Ozawa et al. (2021)
ESAM	BEM	Liu Y.	Segall and Bradley (2012)
EQsimu	FEM	Liu D.	Liu et al. (2020)

Table 3 Parameters in the 2D thrust fault model

	ρ (kg/m^3)	η (Pas)	G (Pa)	Depth (km)	RSF Parameter					
					a	b	D_{RS} *(m)*	μ_{st}^{*}	σ_n (MPa)	V_0 (m/s)
UC	2700	10^{27}	3e10	0-30	0.003	0.001#	0.01	0.3	30	4×10^{-9}
LC	2950	$10^{19\text{-}21}$	3e10	30-45	0.003	0.009	0.01	0.3	30	4×10^{-9}

b linear increases from 0.001 at 27 km to 0.009 at 30 km

Figure1.

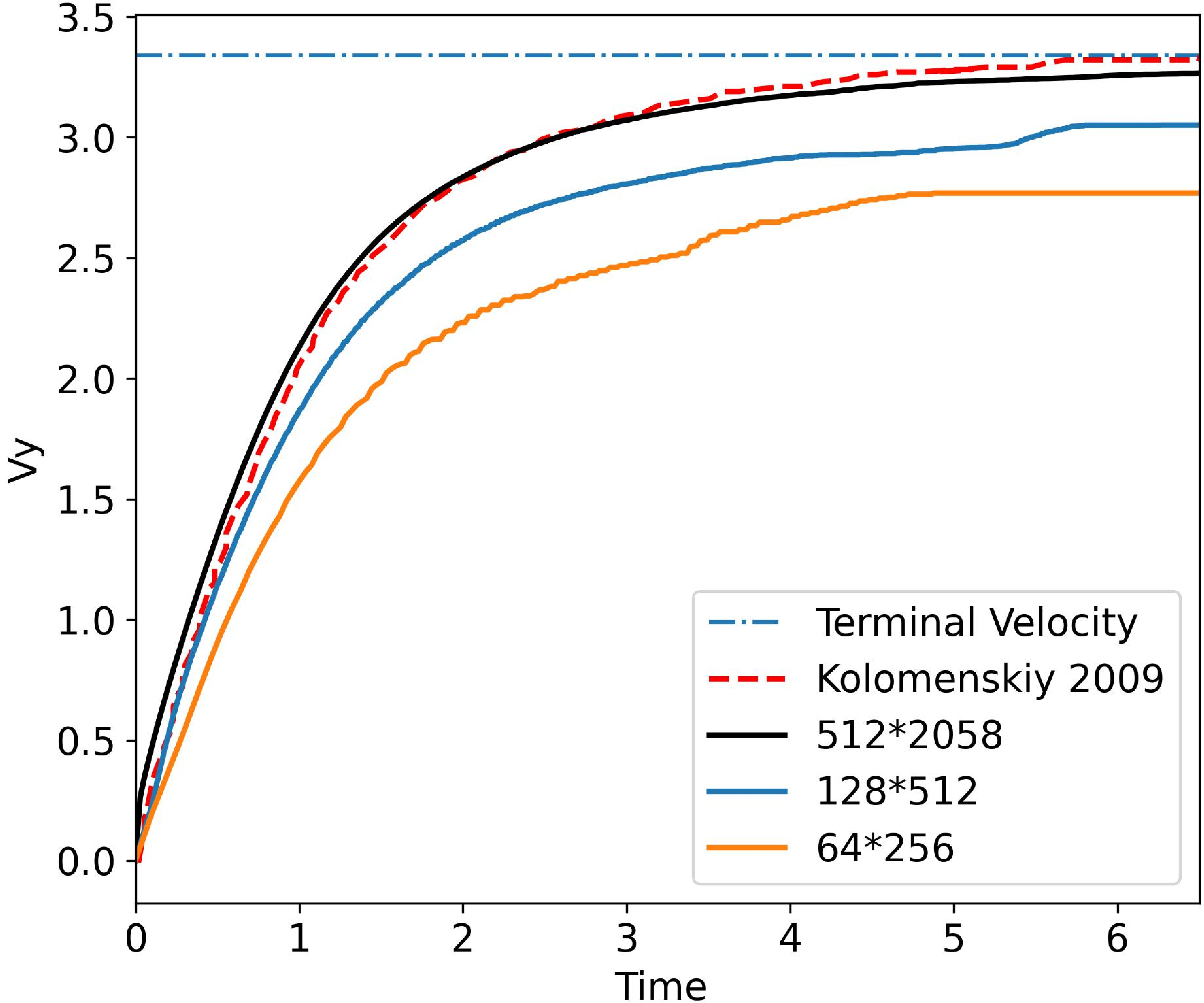
3.5
3.0
2.5
2.0
1.5
1.0
0.5
0.0
Vy
0
1
2
3
4
5
6
Time
Terminal Velocity
Kolomenskiy 2009
512*2058
128*512
64*256

Figure2.

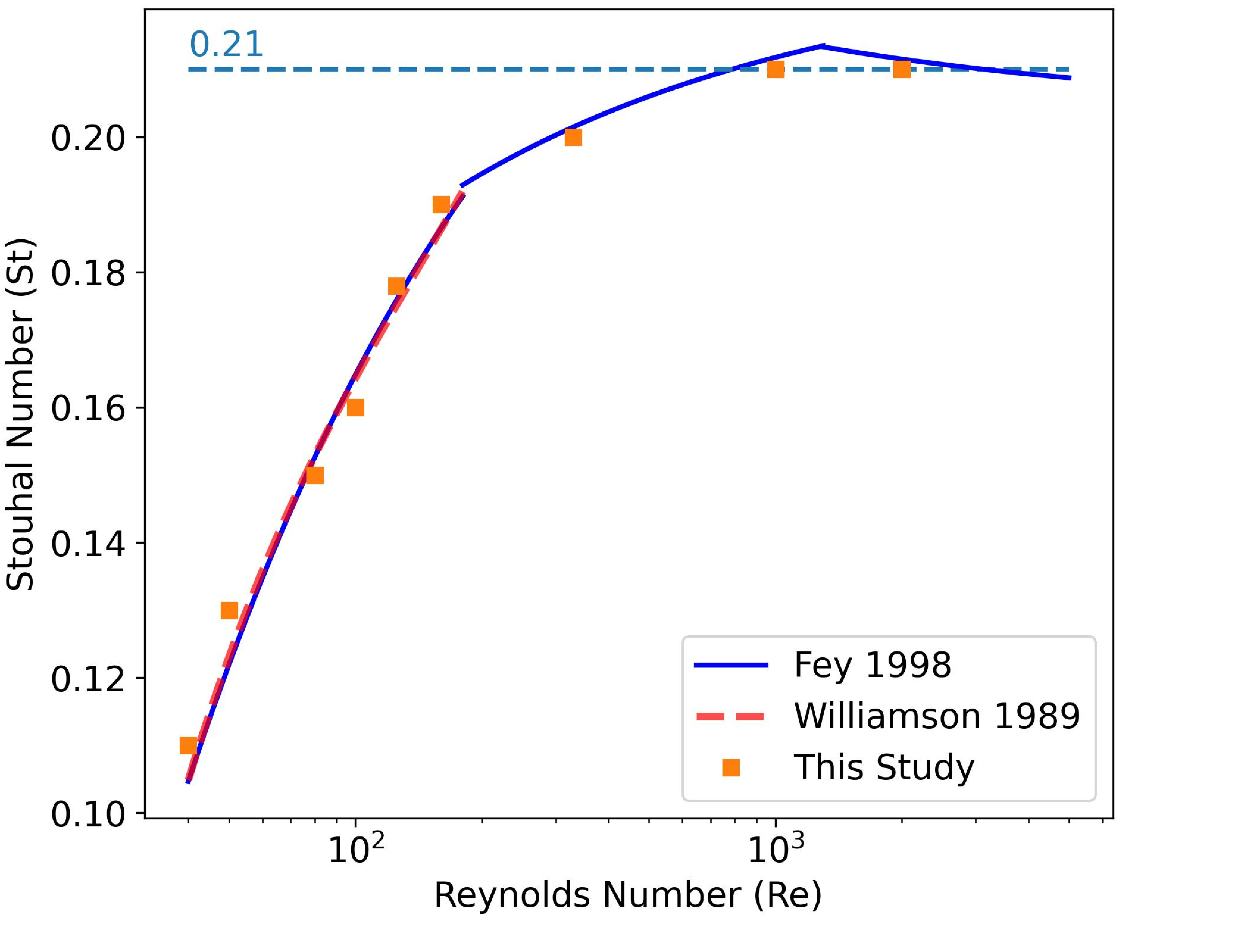

0.21
0.20
0.18
0.16
0.14
0.12
0.10
Stouhal Number (St)
10^2
10^3
Reynolds Number (Re)
Fey 1998
Williamson 1989
This Study

Figure3.

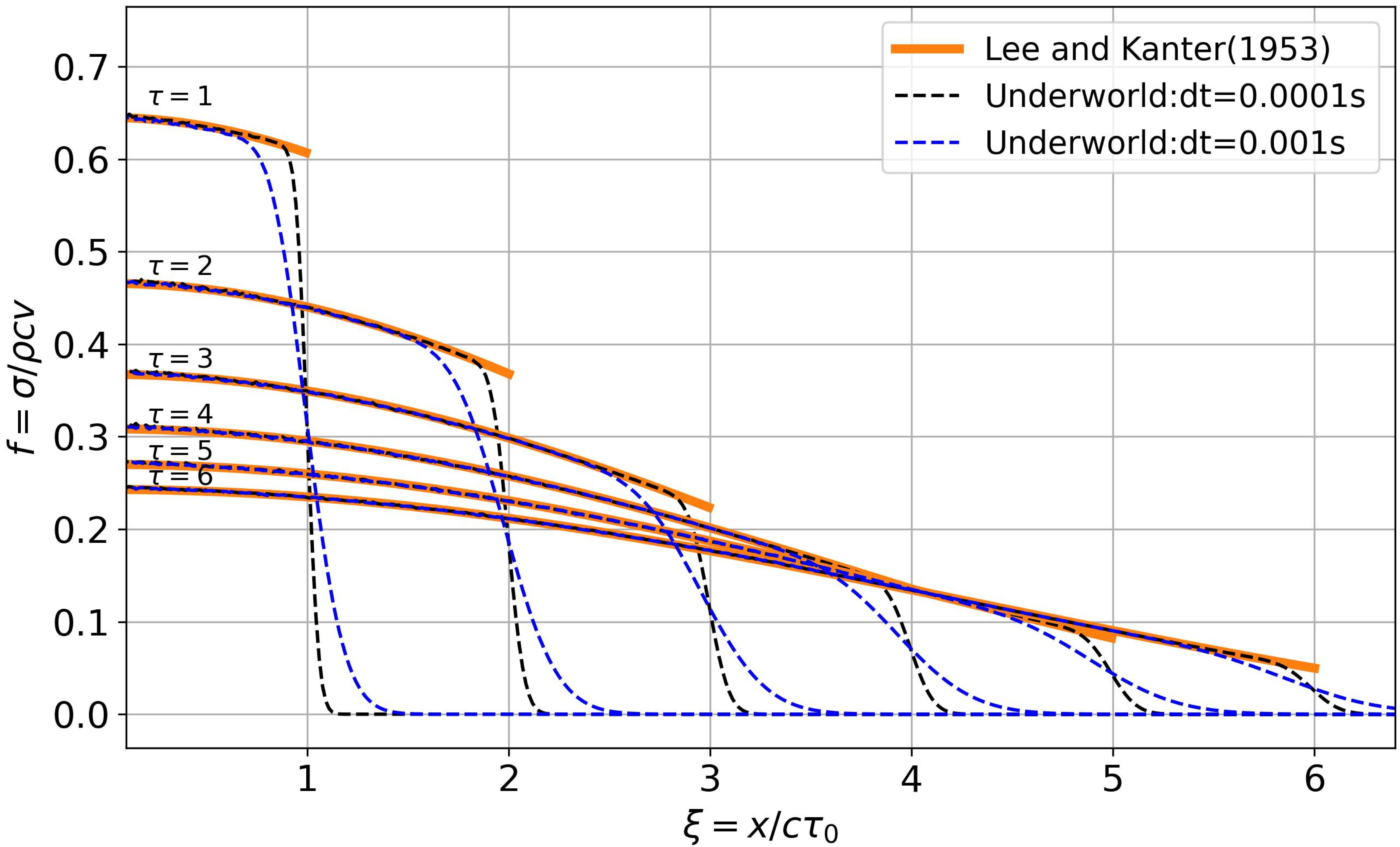

Lee and Kanter(1953)
Underworld:dt=0.0001s
Underworld:dt=0.001s
$\tau = 1$
$\tau = 2$
$\tau = 3$
$\tau = 4$
$\tau = 5$
$\tau = 6$
0.0
0.1
0.2
0.3
0.4
0.5
0.6
0.7
$f = \sigma/\rho c v$
1
2
3
4
5
6
$\xi = x/c\tau_0$

Figure4.

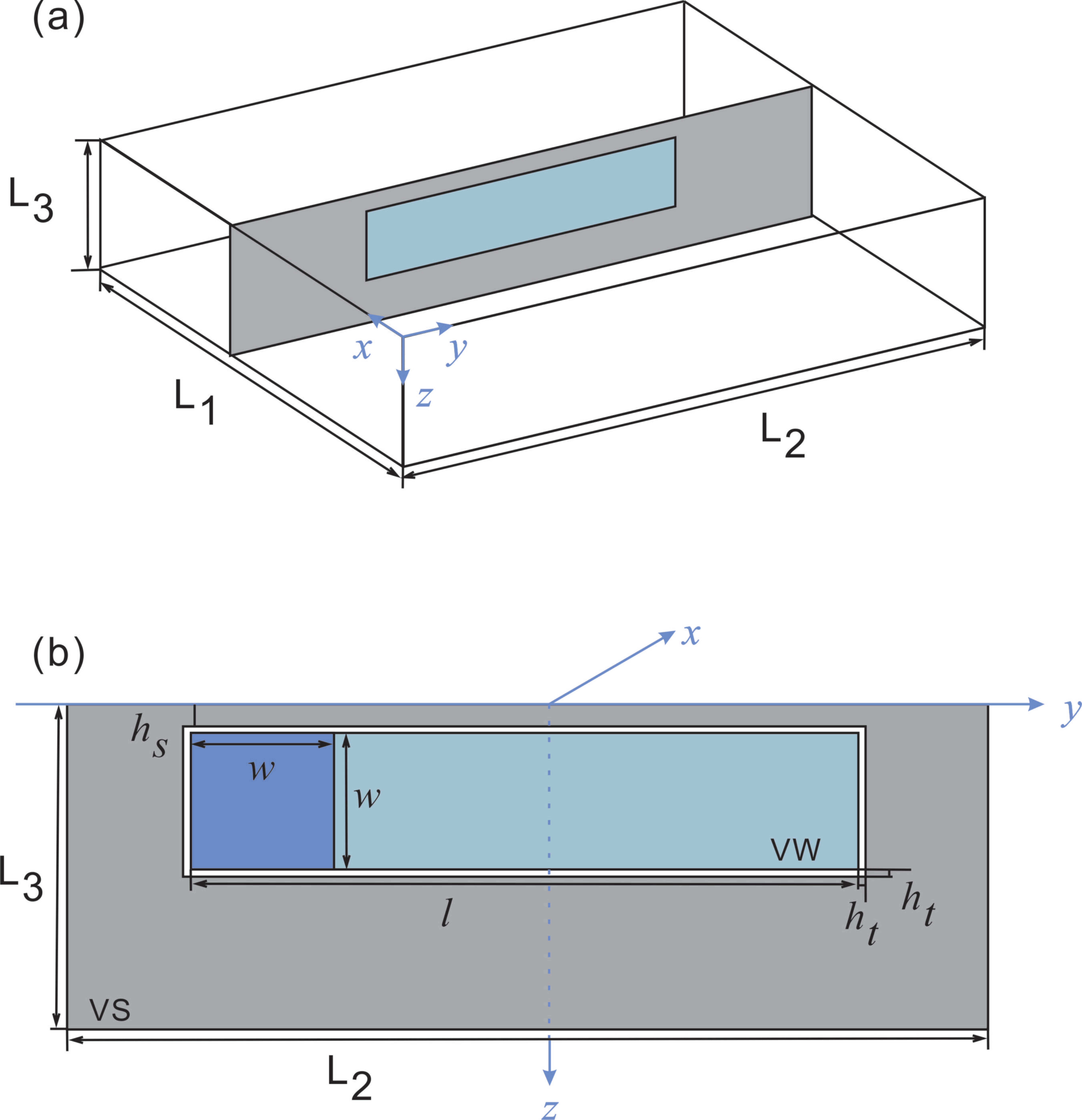

(a)
L3
L1
L2
x
y
z
(b)
x
y
hs
w
w
VW
l
ht
ht
L3
VS
L2
z

Figure5.

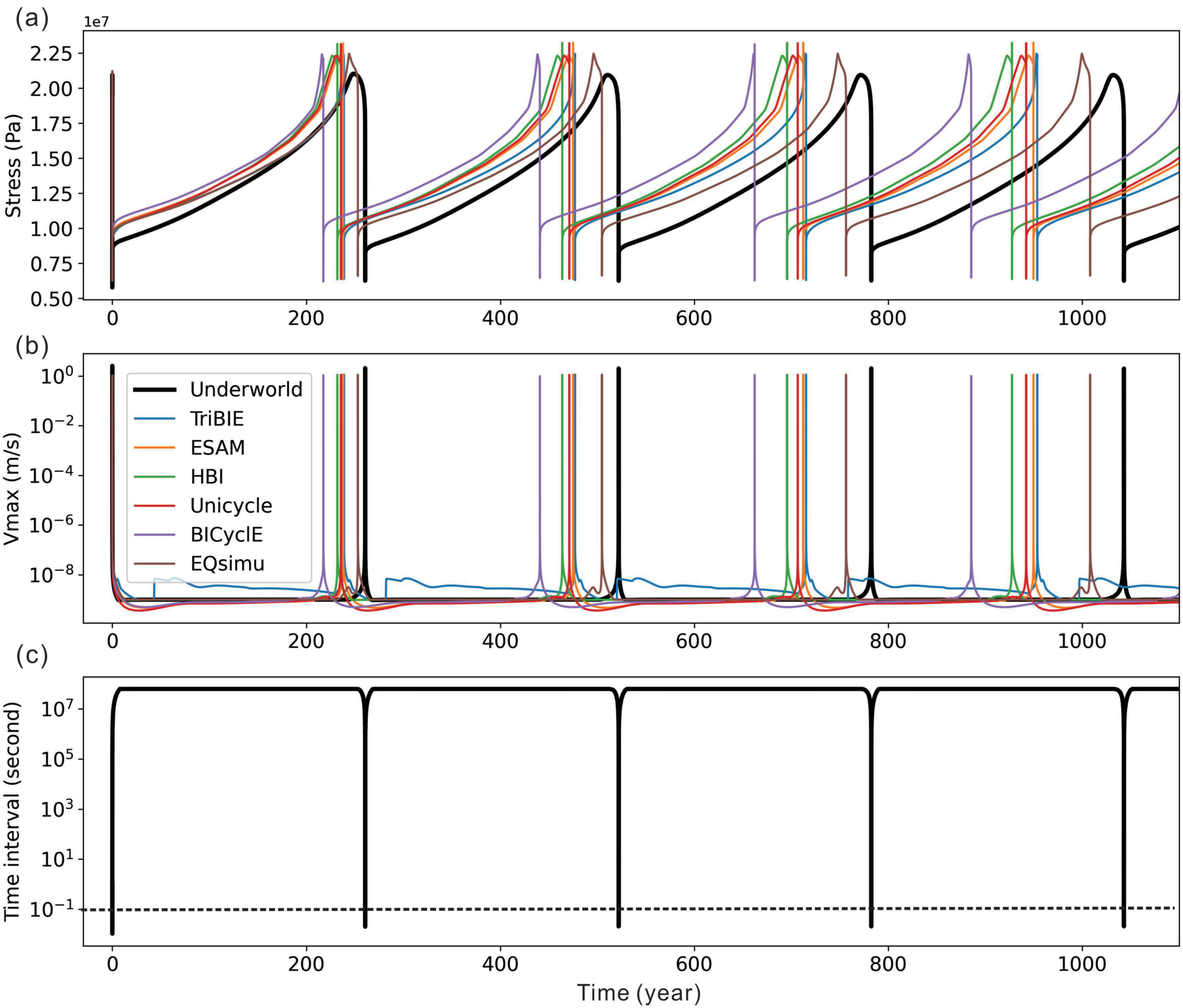

(a)
1e7
Stress (Pa)
2.25
2.00
1.75
1.50
1.25
1.00
0.75
0.50
0
200
400
600
800
1000
(b)
Vmax (m/s)
10^{0}
10^{-2}
10^{-4}
10^{-6}
10^{-8}
Underworld
TriBIE
ESAM
HBI
Unicycle
BICyclE
EQsimu
(c)
Time interval (second)
10^{7}
10^{5}
10^{3}
10^{1}
10^{-1}
Time (year)

Figure6.

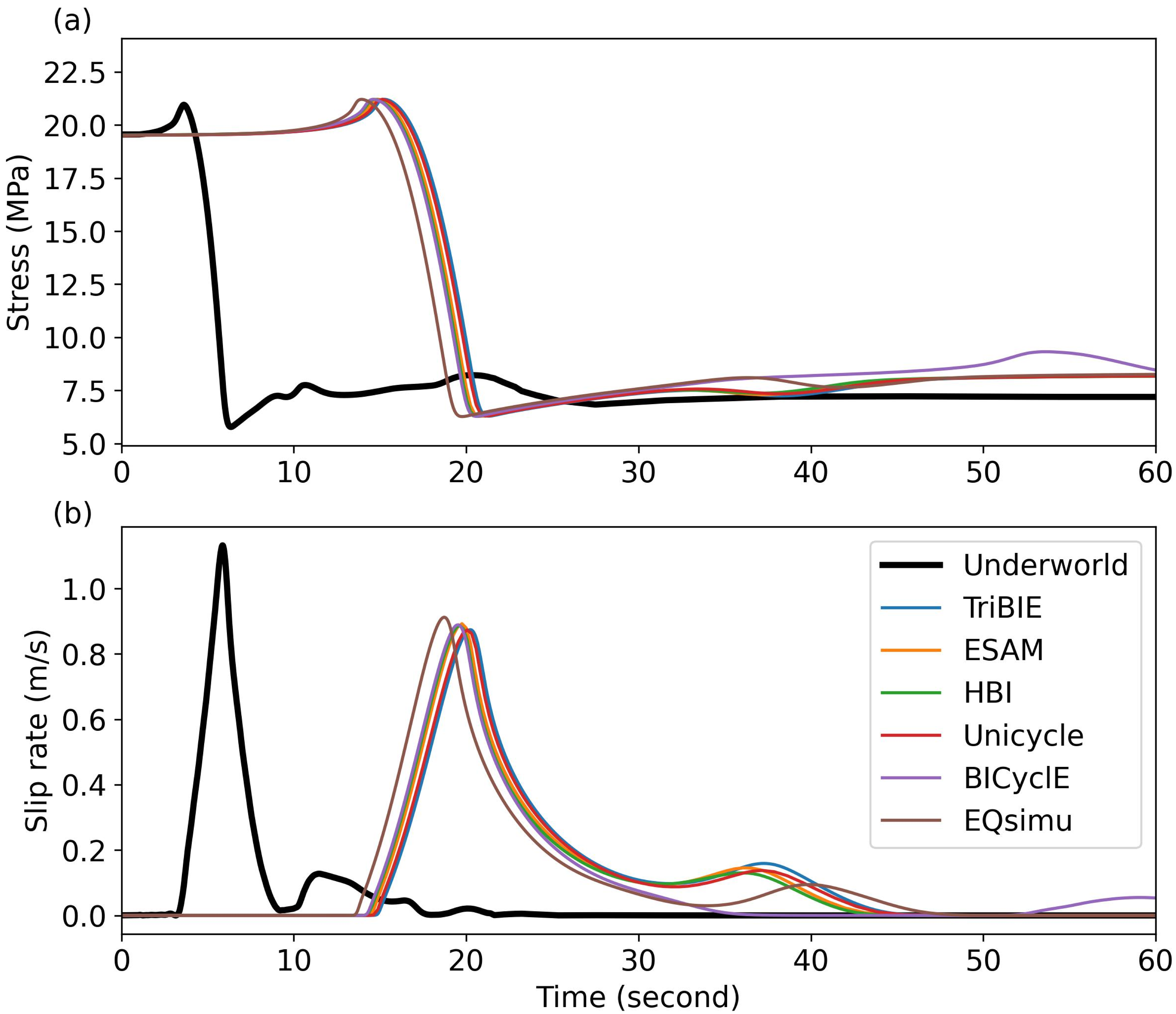
(a)
Stress (MPa)
22.5
20.0
17.5
15.0
12.5
10.0
7.5
5.0
0
10
20
30
40
50
60
(b)
Slip rate (m/s)
1.0
0.8
0.6
0.4
0.2
0.0
Time (second)
Underworld
TriBIE
ESAM
HBI
Unicycle
BICyclE
EQsimu

Figure7.

0
−5
−10
−15
−20
−25
−30
Depth (km)
0
5
10
15
20
25
30
35
40
Displacement (m)

Figure8.

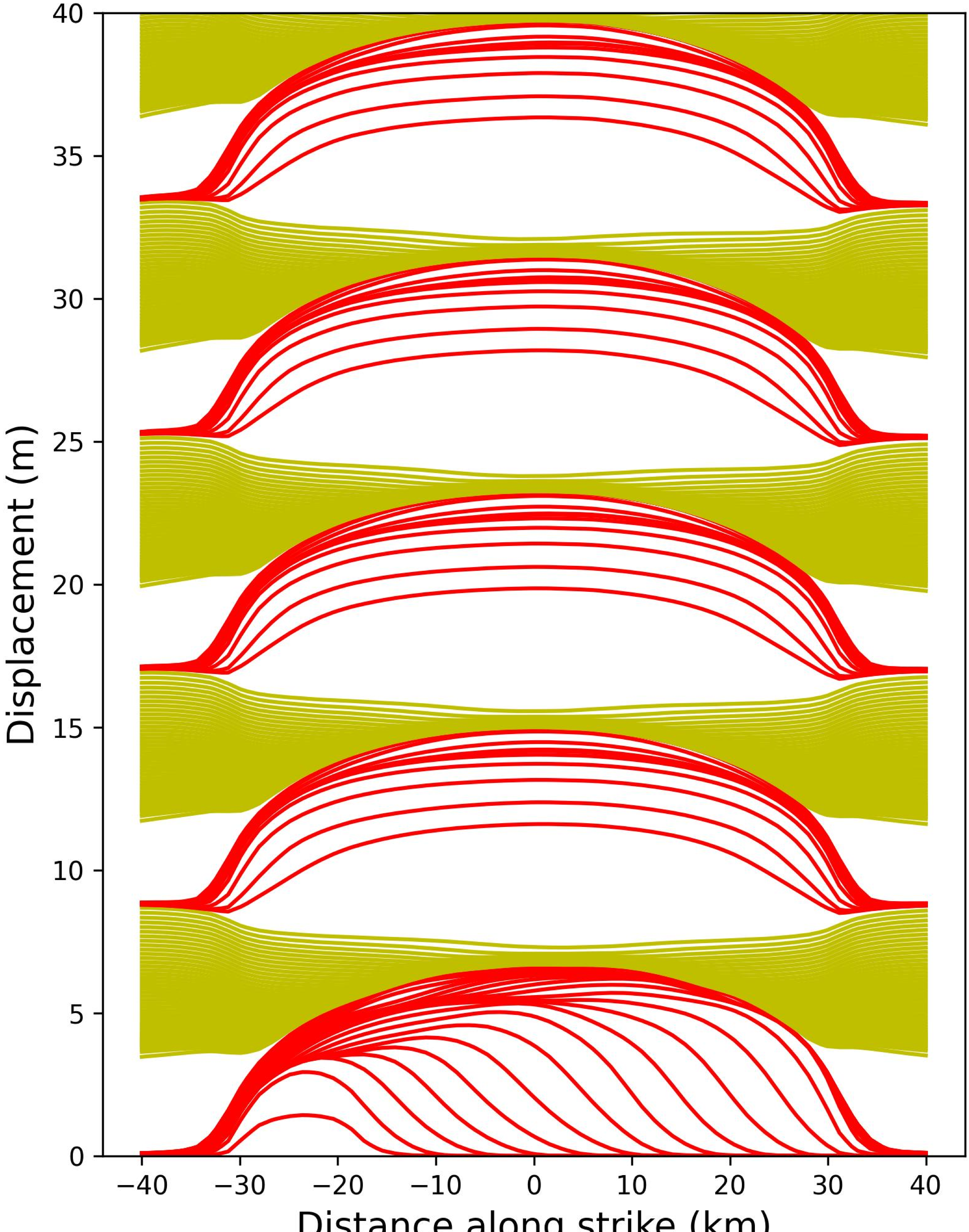

Displacement (m)
Distance along strike (km)
0
5
10
15
20
25
30
35
40
−40
−30
−20
−10
0
10
20
30
40

Figure9.

Depth (km)
Displacement (m)
0
−5
−10
−15
−20
−25
−30
0
5
10
15
20
25
30

Figure10.

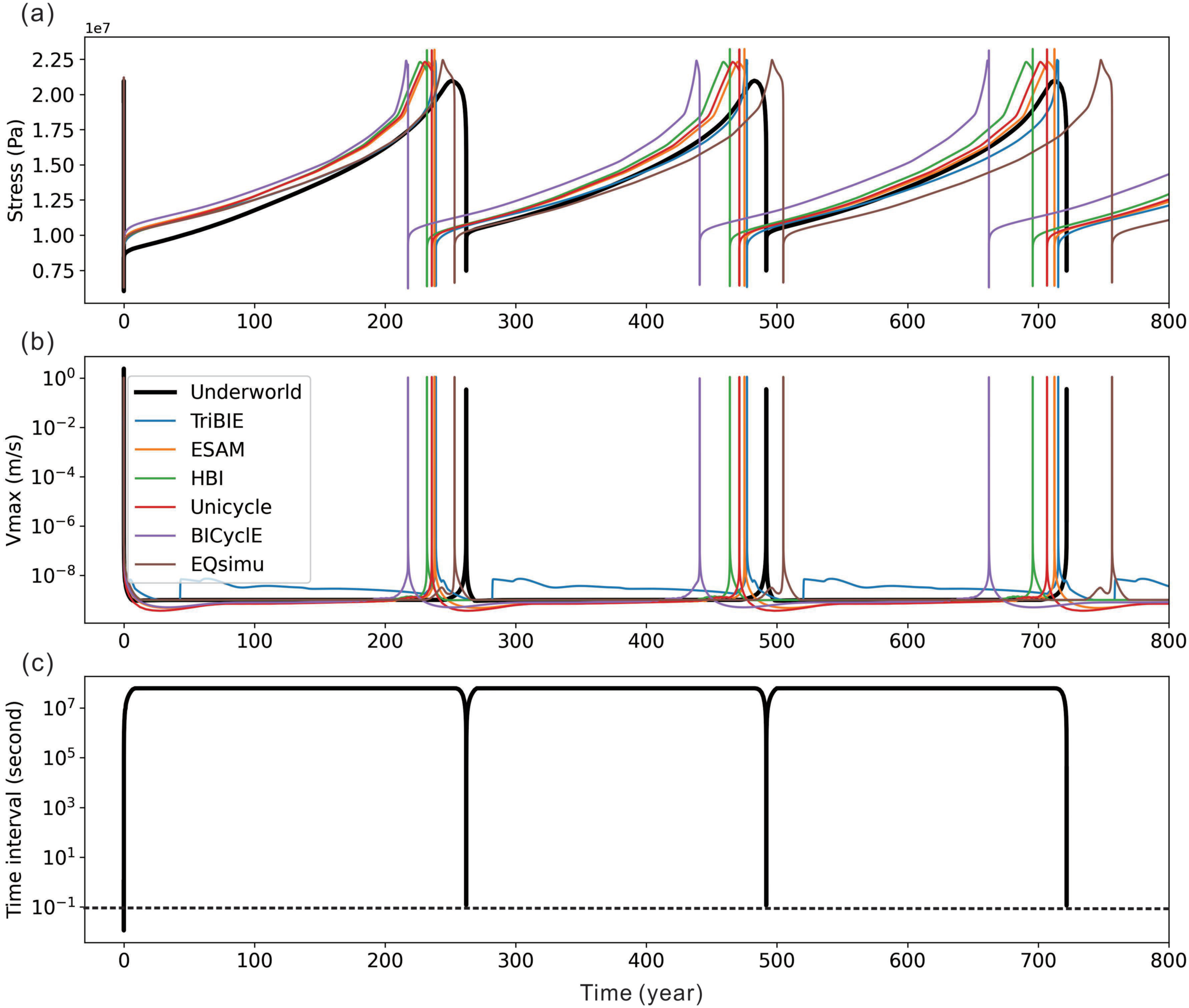
(a)
1e7
Stress (Pa)
2.25
2.00
1.75
1.50
1.25
1.00
0.75
0
100
200
300
400
500
600
700
800
(b)
Vmax (m/s)
10^{0}
10^{-2}
10^{-4}
10^{-6}
10^{-8}
Underworld
TriBIE
ESAM
HBI
Unicycle
BICyclE
EQsimu
(c)
Time interval (second)
10^{7}
10^{5}
10^{3}
10^{1}
10^{-1}
Time (year)

Figure11.

0
15
30
45
Depth (km)
Upper Crust
Case1
Fault zone
VW
Transition zone 3 km
Lower Crust
Case2
VS
-200
-100
0
100
200
Distance (km)

Figure12.

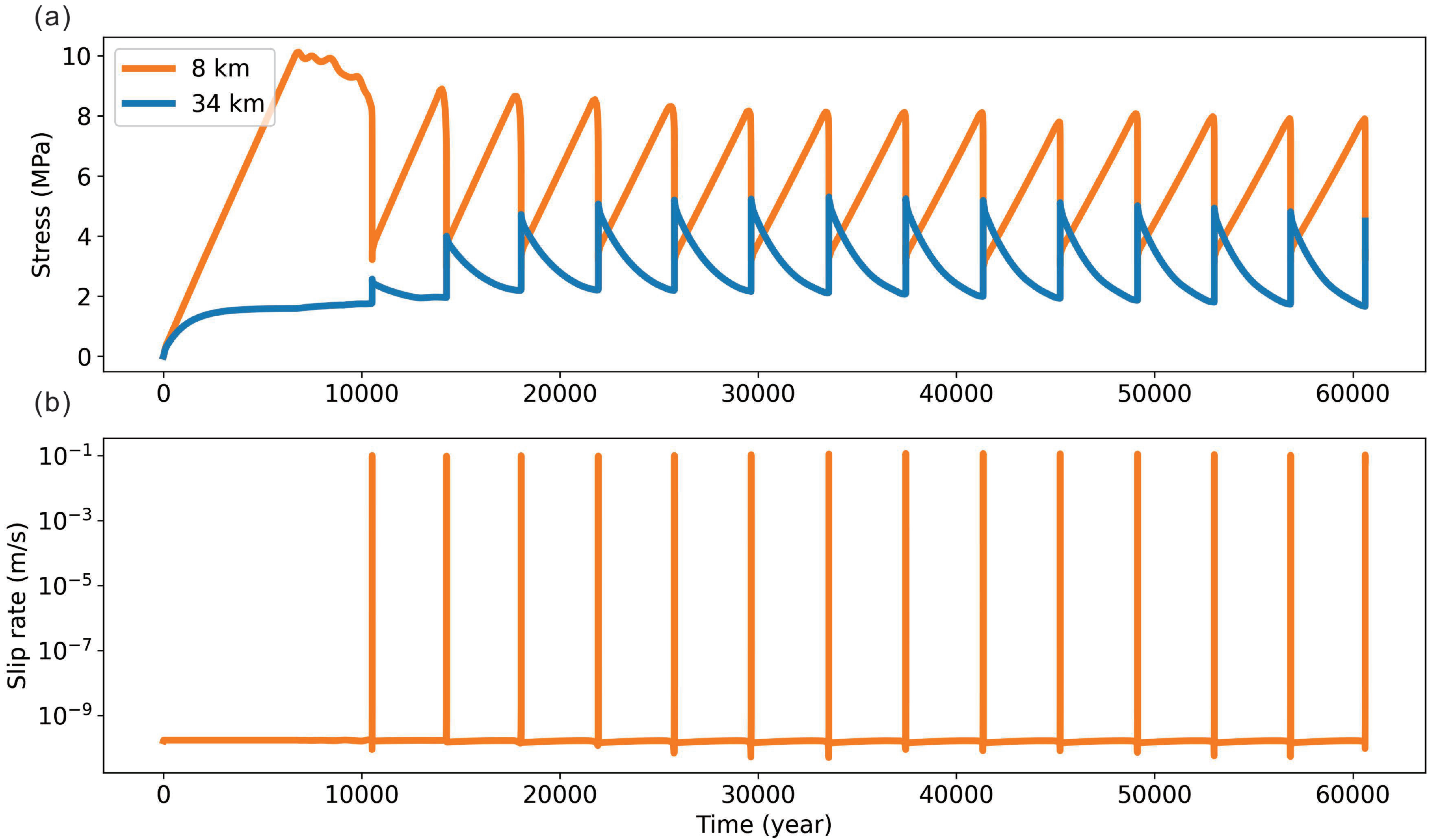

(a)
8 km
34 km
Stress (MPa)
10
8
6
4
2
0
0
10000
20000
30000
40000
50000
60000
(b)
Slip rate (m/s)
10^{-1}
10^{-3}
10^{-5}
10^{-7}
10^{-9}
0
10000
20000
30000
40000
50000
60000
Time (year)

Figure13.

(a)
LC Viscosity = 1e19 Pas, UP
Vx (cm/yr)
Distance (km)
Vz (cm/yr)
16.1yr, 1.53τ
57.3yr, 5.43τ
207.9yr, 19.68τ
716.5yr, 67.85τ
(b)
LC Viscosity = 1e20 Pas, UP
16.4yr, 0.16τ
79.8yr, 0.76τ
111.4yr, 1.06τ
222.4yr, 2.11τ
745.2yr, 7.06τ
(c)
LC Viscosity = 1e21 Pas,UP
10.7yr, 0.01τ
85.8yr, 0.08τ
371.5yr, 0.35τ
971.5yr, 0.92τ
2071.5yr, 1.96τ
(d)
LC Viscosity = 1e19 Pas, LOW
16.7yr, 1.58τ
57.8yr, 5.48τ
208.4yr, 19.73τ
712.2yr, 67.44τ
(e)
LC Viscosity = 1e20 Pas, LOW
15.7yr, 0.1τ
56.6yr, 0.5τ
104.8yr, 1.0τ
202.6yr, 1.9τ
302.0yr, 2.9τ
798.7yr, 7.6τ
(f)
LC Viscosity = 1e21 Pas, LOW
9.5yr, 0.01τ
117.1yr, 0.11τ
301.0yr, 0.29τ
713.7yr, 0.68τ
1055.3yr, 1.00τ